Effect of fO_2 on Eu, Co and Ni partitioning between clinoproxene, orthopyroxene and basaltic melt

Alessandro Fabbrizio[a,*], Max W. Schmidt[b], Maurizio Petrelli[c]

[a]*Institute of Petrology and Structural Geology, Faculty of Science, Charles University, Albertov 6, 12843 Prague, Czech Republic*

[b]*Institute of Geochemistry and Petrology, ETH Zürich, 8092 Zürich, Switzerland*

[c]*Department of Physics and Geology, University of Perugia, Piazza Università, Perugia 06100, Italy*

[*]Corresponding author. *E-mail address:* alessandro.fabbrizio@natur.cuni.cz (A. Fabbrizio).

Abstract

We present partition coefficients for Cs, Li, Sr, Ba, Zn, Mn, Co, Ni, Sc, Ga, Y, La, Nd, Sm, Eu, Tb, Yb, Lu, Ti, Zr, Hf, Ta, Nb and P for synthetic clinopyroxene and orthopyroxene crystallized from a Fe-free basalt at 1.5 GPa and four different oxygen fugacities (fO_2) ranging from 6 log unit above the quartz-fayalite-magnetite oxygen buffer (QFM+6) to QFM-5 at temperatures of 1275-1300 °C. Partition coefficients for the rare earth elements (REEs) vary as a function of their ionic radii, in agreement with lattice strain theory. We use the lattice strain model to evaluate partition coefficients for Eu^{2+} and Eu^{3+}. Our results suggest that fO_2 exerts a primary and important control on Eu, Ni and Co partitioning in clinopyroxene whereas fO_2 seemingly has no recognizable effect on the partitioning behavior of these elements in

orthopyroxene. However, Eu anomalies in orthopyroxene, orthopyroxene Onuma diagrams and calculated proportions of Eu^{2+} in melts show evidences that fO_2 influence Eu partitioning also in orthopyroxene. We combined our results, available experimental data and predictive models for divalent and trivalent Eu clinopyroxene-melt and orthopyroxene-melt partitioning to parameterize fO_2-dependent clinopyroxene-melt and orthopyroxene-melt Eu partitioning models. The reported models reproduce measured Eu partition coefficients within a factor of two. Our model can be applied as clinopyroxene-melt and orthopyroxene-melt oxybarometers if Eu equilibrium partitioning between melt and pyroxene can be demonstrated.

Keywords: Pyroxene; Europium; Oxybarometer; Trace element; Redox conditions; Distribution coefficient

1. Introduction

Magmatic processes are routinely modeled using trace elements mineral-melt partition or distribution coefficients (*D*). If Henry's law is satisfied, partition coefficients will be independent of the concentration of the trace element but highly sensitive monitors to various processes such as fractional crystallization, assimilation, mixing and partial melting of crustal and mantle rocks (e.g., White et al., 2003; Aigner-Torres et al., 2007; Arzilli et al., 2018). Intensive parameters such as mineral and melt compositions, pressure, temperature and redox conditions (fO_2) exert a strong influence on the elements' partitioning behavior. Understanding these effects allows calculation of appropriate *D* values to model and interpret the modeling and process of interest. Trace elements, which valence state varies at magmatic conditions

can be used to constrain the redox state of a magma. More in detail, the quantification of the mineral-melt partitioning behavior of elements that are heterovalent at geological conditions, as well as their relative abundances between oxidized and reduced species have the potential to constitute excellent proxies for the oxidation state of magma and may shed light on the influence of changing redox conditions on the chemical and physical properties of the magma such as volatile solubility, phase equilibria, and viscosity, which in turn will have an influence on the eruptive style of a volcano.

Pyroxenes are a common magmatic rock-forming minerals found both in plutonic, in effusive, as well as in many partially molten high-temperature metamorphic rocks. Pyroxenes, with a general formula $XY(Si, Al)_2O_6$, can host many different cations in their M1 and M2 sites. The coordination is VI- (M1) and VIII-fold (M2) in clinopyroxene (cpx) and VI-fold in orthopyroxene (opx), respectively (Blundy and Wood, 2003). The larger M2 site hosts larger mono-, di-, tri-, and tetra-valent cations (e.g., most alkalis, Ca and REE) whereas the smaller di-, tri-, tetra-, and penta-valent cations (e.g., Ni, Co, Sc, Ti, Zr, Hf) are hosted by the M1 site (Blundy and Wood, 2003; Sun and Liang, 2012, 2013; Yao et al., 2012; Dygert et al., 2014, 2020; Sun, 2018; Baziotis et al., 2019). The main difference between cpx and opx is that the opx VI-fold M2 site is smaller than the equivalent VIII-fold coordinated cpx site (Blundy and Wood, 2003). Consequently most of the commonly used trace elements are more incompatible in opx than in cpx (e.g., Blundy and Wood, 2003; Salters et al., 2002; McDade et al., 2003a,b; Sun and Liang, 2012; Yao et al., 2012).

Among the heterovalent elements, Eu is of particular interest as it is an abundant trace element in pyroxenes and dominantly Eu^{3+} in the range of redox conditions characterizing terrestrial magma (Carmichael, 1991), changing from dominantly Eu^{2+}

to dominantly Eu^{3+} at oxygen fugacities above the iron-wüstite (IW) buffer (Shearer et al., 2006). Both in cpx and in opx, trivalent ions have a favorable partitioning with respect to divalent ions because of the closest match of their ionic radii to the size of the M2-sites, although recent experimental works have shown no preferential incorporation of trivalent rather than divalent Eu in opx (Sun and Liang, 2013; Dygert et al., 2014, 2020). The change of valence from di- to tri-valent in silicate melts can be expressed via the reaction $EuO^{melt} + 0.25O_2^{melt} = EuO_{1.5}^{melt}$. This implies that the relative proportions of Eu^{2+} (EuO) and Eu^{3+} ($EuO_{1.5}$) in a silicate melt will be a function of oxygen fugacity (fO_2) and the magnitude of the resultant Eu anomaly in minerals resulting from different partition coefficients of Eu^{2+} and Eu^{3+} will then record the prevailing redox conditions. Consequently, D_{Eu}, or any D_i of heterovalent elements, can be used to constrain the redox state of a magma (e.g., Aigner-Torres et al 2007; Burnham and Berry, 2012; Trail et al., 2011, 2012; Dygert et al., 2020).

In this study, we report a series of experiments performed at high-temperature, high-pressure and varying fO_2 using a synthetic Fe-free basaltic starting material to better understand how the heterovalent trace elements Eu, Ni, and Co are fractionated between cpx, opx and basaltic melt. The new experimental data for Eu are combined with previously reported ones to parameterize a model for cpx-melt and for opx-melt Eu partitioning as a function of the oxygen fugacity. The proposed models can be used as Eu-in-pyroxene oxybarometers in magmatic systems.

2. Experimental and analytical methods

2.1. Starting composition

An Fe-free basalt was chosen as the starting composition (Table 1) because absence of Fe prevents i) problems with changing ferric/ferrous ratios, ii) crystallization of variable amounts of Fe-Ti oxides, and iii) alloying of Fe to Pt capsules especially at low oxygen fugacities. Furthermore this basalt iv) has phase equilibria that are well known (Mallmann and O'Neill, 2007), v) assures the presence of large amounts of quenched silicate melt in the experiments and vi) has high normative pyroxene contents maximizing the potential for crystallizing large pyroxenes suitable for trace element analysis. A 1 g-batch of the starting mix was prepared by mixing and grinding reagent grade oxides, carbonates and phosphates under ethanol in an agate mortar. The powder was then dried, placed in a Pt crucible, and fired overnight in a 1 atmosphere muffle furnace at 1000 °C. This material was re-ground under ethanol and dried again. A series of selected trace elements (Rb, Cs, Li, Sr, Ba, Zn, Sc, Ga, La, Lu, Eu, Yb, Nd, Y, Sm, Tb, Zr, Hf, Ta, Nb) was added to the starting mix as a mix of oxides, carbonates and chlorides in the amount of totally 1 wt%, resulting in individual concentrations ranging from ~100 to 600 ppm (Table S1), followed by regrinding under ethanol. Nickel and Co oxides were then added to the mix each in the amount of 1 wt%, the mixture was re-ground under ethanol after each addition.

2.2. High-temperature/high-pressure experiments

Experiments were performed at 1275 and 1300 °C, 1.5 GPa using an end-loaded piston-cylinder apparatus with a 14 mm bore at ETH Zürich. Pressure assemblies consisted of an outer talc sleeve wrapped with teflon foil, a Pyrex sleeve, a graphite furnace and inner spacers of crushable magnesia. A friction correction of 10% to nominal pressure was derived from calibration against quartz-coesite at 1000 °C, 3.07 GPa (Bose and Ganguly, 1995) and against fayalite+quartz = orthoferrosilite at 1000 °C, 1.41 GPa (Bohlen et al., 1980). Temperatures were measured with an estimated accuracy of ±5 °C using type B ($Pt_{94}Rh_6$-$Pt_{70}Rh_{30}$) thermocouples protected by a mullite tube. A disk of corundum (0.63 mm thick) was placed between thermocouple tip and capsule to avoid reaction between them. For each run ~20 mg of starting material were loaded in single or double capsules with a final length of ~5 mm.

In order to investigate the full change in oxidation state of Eu as well as Ni and Co, experiments were designed to cover a wide range of redox conditions (fO_2s). Sample containers were either 2 mm Pt capsules (inner diameter, I.D. = 1.7 mm), 3 mm graphite capsules (I.D. = 1.5 mm) or 3.15 mm graphite-lined molybdenum capsules (I.D. graphite = 1.3 mm). Graphite and graphite-lined molybdenum capsules were placed inside 4 mm Pt capsules (I.D. = 3.5 mm) and the free space filled by graphite or Mo-powder. Layers of $Ru+RuO_2$ or $Re+ReO_2$ mixes were placed at the top and bottom of the starting mixture in a sandwich arrangement in experiments carried out in Pt capsules to control fO_2 at conditions close to ~6 log unit above the quartz-fayalite-magnetite oxygen buffer (QFM+6), ~IW+10, ($RuRuO_2$ buffer) or ~QFM+2, ~IW+6, ($ReReO_2$ buffer). The use of graphite capsules constrains the fO_2 to

conditions close to ~QFM-3 or ~IW+1, whereas molybdenum+graphite places the fO_2 at reducing conditions close to ~QFM-5 or ~IW-1 (Dygert et al., 2014). fO_2s were calculated at run temperature and pressure using appropriate buffer equations (Frost, 1991; Pownceby and O'Neill, 1994; O'Neill and Nell, 1997). Post run EDS spectra showed the coexistence of the metal-oxide pairs in the buffer layers, constraining fO_2 to a fixed value.

Some double capsule experiments were performed with an inner Pt capsule containing the starting material and an outer Pt capsule containing a metal-oxide buffer (MnO-Mn_3O_4; Ni-NiO; Fe-FeO) plus liquid water. However, this technique was abandoned because of the difficulties related to the determination of the presence of water in the post-run step and of the diffusion of some elements (i.e., Ni and Co) towards the external buffer.

Experiments were conducted first raising temperature to 1400 °C (super liquidus) and holding this temperature for 1 hour. Then, temperature was decreased to the final temperature with a cooling rate of 2 °C/min, to obtain crystal sizes large enough to be analyzed by laser ablation-ICP-MS. The equilibrium temperature was held for 26-53 hours. Pressure was held constant at 1.5 GPa. Experiments were terminated by cutting off power and quenched to <500 °C within 5 s, the recovered capsules were mounted in epoxy and polished for analyses (EMPA and LA-ICP-MS). Run conditions are reported in Table 2.

2.3. Electron microprobe analysis

Backscatterd electron (BSE) images (Fig. 1) were collected using a JEOL JXA-8530F Electron Microprobe Analyzer (EMPA) at the Institute of Petrology and

Structural Geology, Charles University. Analytical conditions for mineral phases were 15 kV, 100 nA beam current, beam size of 1 μm and count times of 90 seconds on peak for Ni and Co and of 20 seconds for all the other elements with half-times on background. With this setup the detection limits were 0.003 wt% for Co and 0.004 wt% for Ni. Glasses were analyzed using 15 kV accelerating voltage, 10 nA beam current, a beam size of 10 μm and measurement times of 60 seconds on peak for Ni and Co (30 s on background) and 20 seconds for all the other elements (10 s on background). In order to improve analytical precision for Co and Ni concentrations in glasses, these elements were re-measured using longer counting times (90 s on peak, 45 s on background), a higher beam current (200 nA), and a 20-μm beam diameter. The detection limits for Co and Ni lowered between 0.002 and 0.003 wt%. For all oxides, the percentage errors on the measurements calculated from counting statistics were <10% both in the glasses and in the mineral phases. Standards for calibration were quartz for Si, corundum for Al, rutile for Ti, periclase for Mg, rhodonite for Mn, albite for Na, sanidine for K, calcite for Ca, apatite for P, nickel oxide for Ni and pure cobalt for Co. Data reduction was carried out using the ZAF correction. Averages of crystal and glass compositions reported in Table 2 represent minimally zoned portions for crystals that were targeted during laser ablation analysis.

2.4. Laser ablation-inductively coupled plasma mass spectrometry (LA-ICP-MS)

Trace element analyses were carried out at the Department of Physics and Geology, Perugia University, by Laser Ablation Inductively Coupled Plasma Mass Spectrometry (LA-ICP-MS) using a Teledyne/Photon Machine G2 LA device equipped with a Two-Volume ANU HelEx 2 cell coupled with a Thermo Fisher

Scientific iCAP Q, quadrupole-based, ICP-MS. Analyses were performed by using a circular laser beam with a frequency of 8 Hz and a laser density on the sample surface of 3.5 J/cm^2. A beam diameter of 50 μm diameter was used for pyroxene crystals, except in sample 16 were only 20 μm were feasible. Glasses were analyzed with a beam diameter of 110 μm. Data Reduction was carried out following the procedure reported by Longerich et al. (1996), and using the Iolite v.3 software package (Paton et al., 2011). The standard reference glass NIST SRM-610 was used as calibrant with Ca, previously analyzed by EMPA, utilized as internal standard. The USGS BCR2G natural reference material was analyzed as unknown to monitor data quality. Under these operating conditions precision and accuracy are better than 10% for all elements (Günther et al., 1997; Petrelli et al., 2007, 2008, 2016a, 2016b). Glass contamination in mineral analyses was identified by a careful screening of time resolved signals and the section of the signal that showed a sudden increase in the rare earth elements (REEs) was removed during data reduction. Contamination by glass, i.e., melt inclusion or glass underlying crystal, is easily recognized by observing spikes in the elemental signal of highly incompatible elements (e.g., La for pyroxene). Averaged trace element concentrations are reported in Table 2.

3. Results

3.1. Run products

A summary of experimental conditions, run products and average chemical compositions is given in Table 2, representative BSE images images provided in Fig. 1. Glass is the predominant phase followed by abundant cpx and opx and in some runs

minor presence of forsterite and spinel. The different mineralogical assemblages obtained at the same temperature but variable fO_2 suggest that redox conditions influence the liquidus also in Fe-free systems. With decreasing fO_2 assemblages were melt-only, opx+melt, cpx+opx+melt, and cpx+opx+fo+sp+melt at 1300 °C and cpx+opx+fo+sp+melt and opx+melt at 1275 °C. In all experimental run products, pyroxenes are euhedral/subhedral ranging from 40 to 100 μm in narrowest dimension. Forsterite and spinel crystals developed euhedral/subhedral shapes reaching 20 μm in size. In general, crystals are homogenously distributed and immersed in large pools of silicate melt quenched to glass, suggesting minor thermal gradients. Some opx crystals have (sub)micrometer acicular quench rims and most cpx grains have a micrometer wide rim infered to form during quenching. Electron microprobe analyses (Table 2) demonstrate that pyroxene crystals do not exhibit major element zonation and the low standard deviation of major- and trace-element analysis testify for their homogeneity. All minerals and glass data were acquired from spots well away from quench rims. Cpx are augitic and range from $En_{47}Wo_{43}$ (run 23) to $En_{63}Wo_{37}$ (run 25), whereas opx have a more limited variability from $En_{96}Wo_4$ (runs 13, 21, 23, 25) to $En_{98}Wo_2$ (run 24). Olivine crystals are pure forsterite and spinel crystals are Al-spinels. In the more oxidized charge (run 23) forsterite and spinel crystals have up to 8 wt% NiO+CoO. The observed variations in glass compositions between runs reflect the crystallization of different phases and phase proportions. Silicate glasses are all grossly basaltic in composition, based on normalized total alkalis-silica content, except for one basaltic andesite composition (run 24). Their low totals (95-97 wt%) are likely due to the H_2O, which may result from the hygroscopic nature of the starting materials or from diffusion of H from the piston cylinder assembly into the experimental charges.

3.2. Equilibrium

Evidence that equilibrium conditions were approached stems from: (i) the chemical homogeneity of phases in major and trace elements (Table 2); (ii) run durations comparable to those of previous studies that reached equilibrium (e.g., Mallmann and O'Neill 2007; Sun and Liang, 2012; Dygert et al., 2014); (iii) the absence of significant kinetic effects such as melt inclusions and concentric or sector zoning; (iv) phase assemblages similar to those reported by Mallmann and O'Neill (2007) at comparable *P-T-f*O_2 conditions; and (v) the agreement of temperatures calculated using the Ca-Mg cpx-opx exchange equilibrium of Brey and Köhler (1990) and experimental temperatures (Fig. 2)

3.3. Partition coefficients

Partition coefficients ($D^{pyroxene/melt}$) for cpx and opx in each experimental run are summarized in Table 3 and graphically displayed according to element groups with increasing compatibility in Fig. 3. Partition coefficients for forsterite and spinel are not presented as their limited crystal size did not permit to obtain reliable results.

3.3.1. Clinopyroxene

Variations in the measured $D^{cpx/melt}$ are small among the four experimental charges crystallizing cpx (Fig. 3a). Large ion litophile elements (LILE) are always incompatible with incompatibility decreasing from Ba to Na. Rare earth elements (REE) have an increasing compatibility from La to Lu and approach compatibility (D≈1) with Y and the heavy rare earth elements (HREE) (Fig. 3a,b). The change in

fO_2 from the $RuRuO_2$ buffer to below the IW buffer exerts no obvious influence on D_{REE}, with the exception of D_{Eu}. In the three experiments performed at fO_2 from the $ReReO_2$ buffer to below the IW buffer, Eu is more incompatible than Sm interrupting the increasing trend of compatibility from La to Lu. At the most oxidizing conditions ($RuRuO_2$ buffer), Eu is more compatible than Sm yielding a smooth continuous increase in compatibility from La to Lu. This trend indicates that trivalent Eu is dominant at the most oxidizing conditions and that the cpx crystal structure favors the incorporation of Eu^{3+} over Eu^{2+}. The strength elements (HFSE) are always incompatible, with incompatibility decreasing from Nb to Ti (Fig. 3a). The 1st row transition metals (i.e., Mn, Zn, Sc, Co and Ni) plus Li and Ga tend to switch their behavior from incompatible to compatible with Mn whereas Ni is the most compatible element (Fig. 3a).

3.3.2. Orthopyroxene

As in the case of cpx, the trends in measured $D^{opx/melt}$ are similar among the six experiments crystallizing opx (Fig. 3a). Partition coefficients values for LILE are one order of magnitude lower than for cpx. Calculated D_{Ba} values are affected by large errors (Fig. 3a) due to its high incompatibility (i.e., a very low concentration in the opx) and the analytical difficulty to obtain reliable data. Also, any contamination with glass during pyroxene ablation affects the apparent Ba-concentration much more than for the less incompatible Sr and Na. REE are more incompatible than in cpx. In detail, $D_{La}^{opx/melt}$ values are 18-90 times lower than $D_{La}^{cpx/melt}$, the difference decreasing from light to heavy REE, $D_{Lu}^{opx/melt}$ values are only 3-6 times lower than for cpx (Fig. 3a,b). The most incompatible (La) is the most difficult to measure and results in relatively large errors in D_{La}. The changing redox conditions exert a measurable influence only

on D_{Eu}. In the most oxidized runs ($ReReO_2$ and $RuRuO_2$ buffers) REE show a smooth continuous increase in their compatibility, whereas in the reduced runs (graphite and graphite-lined molybdenum capsules) Eu is more incompatible than Sm reflecting the higher proportion of Eu^{2+} in the melt. Partition coefficient values for HFSE show a more incompatible behavior than in cpx with $D_{Nb}^{opx/melt}$ 5-17 times lower than $D_{Nb}^{cpx/melt}$ and $D_{Ti}^{opx/melt}$ 2-5 times lower than $D_{Ti}^{cpx/melt}$ (Fig. 3a). The 1st row transition metals plus Li and Ga in opx do not show any significant difference with respect to cpx (Fig. 3a).

4. Discussion

4.1. Interpretation of the experimental data by application of the lattice strain model

On a given crystallographic site, the mineral/melt partition coefficient D_i of element i with ionic radius r_i can be related to the partition coefficient D_0 and ionic radius r_0 of an idealized, optimally fitting element via the lattice strain model equation:

$$D_i = D_0 \exp\{-910.17\, E\, [\tfrac{1}{2}\, r_0\, (r_i - r_o)^2 + \tfrac{1}{3}\, (r_i - r_o)^3] / T\} \qquad (1)$$

where E is the apparent Young's modulus in GPa of the site of interest and T is the temperature in Kelvin (Brice, 1975; Blundy and Wood, 1994, 2003). Eq. (1) applies to elements of the same valence partitioning into the same crystallographic site. The parameters D_0, r_0 and E define an asymmetric parabola with an apex located at (r_0, D_0) and a width determined by the apparent Young's modulus E of the specific

crystallographic site. In other words, E it is a measure of the elastic response of the crystallographic site to lattice strain caused by elements of non-ideal size and hence describes the flexibility of the site (Blundy and Wood, 2003).

The lattice strain model also serves to evaluate the quality of an experimental dataset and to estimate D values of not measured elements. Furtermore, the lattice strain parabola may also be used to (re)evaluate ideal D values for highly incompatible elements such as e.g. La, which low concentrations (in pyroxenes) are problematic in terms of analytical uncertainty and possible contamination by tiny melt inclusions (e.g., van Kan Parker et al., 2011; Dygert et al., 2020). Furthermore, trace elements with partition coefficients $\leq 10^{-3}$ may be influenced by defect substitutions, by surface kinetics and boundary layers in the melt, rendering their experimental determination difficult to impossible (Beattie 1994; Pinilla et al., 2012).

Lattice strain modeling can further be used to evaluate whether elements substitute into multiple sites (e.g., Ba in amphiboles; Tiepolo et al., 2007) or change their valence with oxygen fugacity (e.g., Eu in plagioclase; Aigner-Torres et al., 2007; V, Cr, and Ti in pyroxenes; Cartier et al., 2014). In such cases elements fall off the parabolas defined by elements that substitute exclusively on a given site with a given valency (Dygert et al., 2020).

We recalculated D_{Eu}^{2+} and D_{Eu}^{3+}, following the methodology (supplementary material) described by Aigner-Torres et al. (2007), using a rearranged version of Eq. (1) in which D_0 and r_i are replaced respectively by the measured partition coefficient and ionic radius of Sr to calculate D_{Eu}^{2+} and of another REE^{3+} (preferably Sm or Gd) for D_{Eu}^{3+}, and $r_o^{(2+, 3+)}$ and $E^{(2+, 3+)}$ are estimated by the relationships of Blundy and Wood (2003). This method allowed us fitting the recalculated D_{Eu}^{2+} with other divalent cations and the recalculated D_{Eu}^{3+} with other trivalent cations. The DOUBLE

and SIMPLE FIT programs of Dalou et al. (2018) were used to derive the D_0, r_o and E parameters for each experimental charge and the resulting parabolas on the plane D vs. ionic radius permitted to assess the fit of the data to the model.

4.1.1. Lattice strain parabola of clinopyroxene

The parabolic distribution of the REE partition coefficients suggests that equilibrium conditions were approached in all runs (Fig. 4). Partition coefficients for di- and tri-valent Europium were recalculated as described above and included respectively with divalent and REE elements. Trivalent elements entering the M1 site describe tighter parabolas due to the lesser flexibility of M1 site with respect to M2. In most runs D_{Ba} is characterized by high uncertainties and falls off the parabolas defined by more compatible divalent elements, and was excluded from the fit. Divalent elements entering the M1 site fall on the same side of the M1 – di-valent parabola, hence does not allow to constrain the lattice site parameters (Dalou et al., 2018). Tetravalent elements are hosted in the M1 site and, as expected, their higher charge yields a tighter parabola. The fitted lattice strain parameters for isovalent elements entering in the same site are similar among all experiments (Table 4). Measured REE partition coefficients are in excellent agreement with those calculated using the model of Sun and Liang (2012), (Fig. 5a).

4.1.2. Lattice strain parabola of orthopyroxene

The parabolic trends for isovalent elements have features similar to those described for clinopyroxene (Fig. 6). Nevertheless, REE in low-Ca pyroxene fall on the high radius side of the M2 – trivalent parabola, the apexes are hence not well defined. We have again recalculated D_{Eu}^{2+} and D_{Eu}^{3+} and included the resulting

partition coefficients with the divalent and REE elements on M2. Small trivalent cations prefer the M1 site describing a tighter parabola than that for the larger trivalent cations partitioning into the M2 site (e.g., Frei et al., 2009; van Kan Parker et al., 2010; Sun and Liang, 2013). The good agreement of the experimentally determined REE partition coefficients with their parabolic fits and the good reproducibility (Fig. 5b) of REE distribution coefficients with those calculated by the model of Yao et al. (2012) are suggestive of chemical equilibrium, although the latter tends to underestimate D_{La} with respect to our experimental values. Larger divalent cations prefer the M2 site and describe parabolas of wider shape. Again, experimental D_{Ba} values are generally too high with respect to the expected value on the parabola (~10^{-4}), which relates to the difficulties with very low *D*-values described above. Barium partition coefficients were excluded from the fits. Tetra-valent cations enter in the M1 site defining the tightest parabolas with the highest *E* values as also observed by Sun and Liang (2013). Lattice strain parameters for the opx are reported in Table 4 and fall within the range of values obtained previously (e.g., Yao et al., 2012; Sun and Liang, 2013; Dygert et al., 2020).

4.2. Effect of fO_2 on D_{Eu}, D_{Co}, D_{Ni}

The results of this study permit to evaluate the effect of changing redox conditions on the partitioning behavior of Eu, Ni and Co in cpx and in opx. For cpx, evident linear trends are shown by the D_{Eu}, D_{Co}, D_{Ni} values when plotted as a function of log fO_2 (Fig. 7a). In detail, D_{Eu} correlates positively with oxygen fugacity whereas Ni and Co become less compatibile when moving from reduced to oxidized conditions. These opposite trends imply that cpx structure hosts more easily Eu^{3+}

rather than Eu^{2+}, whereas for Ni and Co the oxidized species are rejected by the cpx structure.

The lattice strain parabola (Fig. 4) for divalent cations in the (smaller) M1 site is not well constrained, because of the paucity of data, but divalent Co and Ni have ionic radii similar to the (in the Fe-free system only) major occupant Mg^{2+}. It is evident that a small lattice site such as the octahedral M1 site of cpx is very resistant to the accommodation of trivalent ions (i.e., Co^{3+} and Ni^{3+}), thus favoring the incorporation of divalent Co and Ni. For the M2 site, the di-valent lattice strain parabola has its apex to smaller radii then Ca, hence the much larger Eu^{2+} is relatively incompatible. Instead the tighter tri-valent M2-site parabola has Eu^{3+} much closer to its apex (near Y) and hence Eu^{3+} is more compatible than Eu^{2+}.

For opx no clear dependencies on oxygen fugacity are shown by the D_{Eu}, D_{Co}, or D_{Ni} (Fig. 7b). This would imply no preferential substitution of divalent rather than trivalent Eu, Co and Ni into the opx structure, which is rather surprising as in four experimental charges opx coexists with cpx for which variations of D_{Eu}, D_{Co} and D_{Ni} values with fO_2 have been observed. Accordingly, a relationship between D_{Eu}, D_{Co}, D_{Ni} and fO_2 would be expected. A series of observations strongly suggest that fO_2 influences at least D_{Eu} also in opx: i) europium anomalies shown in Fig. 3, ii) the parabolas (Fig. 6) for di- and tri-valent cations of runs at reduced conditions (run 13, 21, 25) do not include, respectively, Eu^{2+} and Eu^{3+}, whereas iii) those for trivalent cations of runs at oxidized conditions (run 16, 23, 24) include Eu^{3+}, and Eu^{2+} is again out of the fit for divalent cations, iv) the calculated proportion of Eu^{2+} in melt (Table 4) show a variation with fO_2 (Fig. S1), and v) in runs with two pyroxenes the amount of Eu^{2+} in melt calculated with D_{Eu} data for cpx and opx are comparable (Table 4, Fig. S1).

4.3. A model for describing the partitioning behavior of Eu as a function of fO_2

The mineral/melt partition coefficient for Eu includes a contributions from di- and tri-valent Eu:

$$D_{\mathrm{Eu}} = \{[M_{Eu}{}^{2+}]_{min} + [M_{Eu}{}^{3+}]_{\mathrm{min}}\}/\{[M_{Eu}{}^{2+}]_{\mathrm{melt}} + [M_{Eu}{}^{3+}]_{\mathrm{melt}}\}, \quad (2)$$

where square brackets indicate mass fraction. On the basis of the redox reaction

$$Eu^{3+}O_{1.5} = Eu^{2+}O + 0.25\ O_2, \quad (3)$$

the partitioning model for D_{Eu} between plagioclase and silicate melt was previously parameterized as a function of $f\mathrm{O}_2$ (e.g., Weill et al., 1974; Drake, 1975; McKay et al., 1994; Wilke and Behrens, 1999; Aigner-Torres et al., 2007; Dygert et al., 2020). Here we apply the same parameterization for D_{Eu} of the cpx-melt and opx-melt pairs. The equilibrium constant (K) for Eq. (3) can be written as:

$$K = a\ (Eu^{2+}O)\ (\ f\mathrm{O}_2)^{0.25} / a(Eu^{3+}O_{1.5}), \quad (4a)$$

where a is the activity of the reduced and oxidized species in the melt. This equation can be expanded to include mol-fractions (x) and activity coefficients (γ) into

$$K = x(Eu^{2+}O)\ \gamma(Eu^{2+}O)\ (\ f\mathrm{O}_2)^{0.25} / (x(Eu^{3+}O_{1.5})\gamma(Eu^{3+}O_{1.5})). \quad (4b)$$

Assuming that in the melt the activity coefficients γ are the same for the reduced and oxidized Eu species we obtain

$$K = x(Eu^{2+}O)\,(fO_2)^{0.25} / (x(Eu^{3+}O_{1.5})). \quad (5)$$

A conversion from mole to mass fraction Eq. (5) yields:

$$K = [M_{Eu2+}]_{melt}\,(fO_2)^{0.25} / [M_{Eu3+}]_{melt}. \quad (6)$$

Rearranging and substituting Eq. (6) into Eq. (2), an expression permitting to calculate D_{Eu} as a function of the di- and tri-valent Eu partition coefficients, fO_2, and the equilibrium constant is obtained (e.g., Dygert et al., 2020):

$$D_{Eu} = [K \cdot D_{Eu}^{2+} + D_{Eu}^{3+}(fO_2)^{0.25}] / [K + (fO_2)^{0.25}], \quad (7)$$

where D_{Eu}^{2+} and D_{Eu}^{3+} are distribution coefficients for di- and tri-valent Eu between the mineral cpx or opx in our case, and melt. The rearranged equations of the lattice strain model (supplementary material)

$$D_{Eu}^{2+} = D_{Sr}\exp\{-910.17E^{2+}\,[½r_0^{2+}(r^2_{Sr} - r^2_{Eu}{}^{2+}) + ⅓(r^3_{Eu}{}^{2+} - r^3_{Sr})]/T\} \quad (8a)$$

$$D_{Eu}^{3+} = D_{Sm}\exp\{-910.17E^{3+}[½r_0^{3+}(r^2_{Sm} - r^2_{Eu}{}^{3+}) + ⅓(r^3_{Eu}{}^{3+} - r^3_{Sm})]/T\} \quad (8b)$$

with r_{Sr} = 1.18 Å, r_{Eu}^{2+} = 1.17 Å, r_{Eu}^{3+} = 0.947 Å and r_{Sm} = 0.958 Å in VI-fold coordination (orthopyroxene) and r_{Sr} = 1.26 Å, r_{Eu}^{2+} = 1.25 Å, r_{Eu}^{3+} = 1.066 Å and r_{Sm} = 1.079 Å in VIII-fold coordination (clinopyroxene) (Shannon, 1976)

$$D_{Eu}^{2+\,cpx/melt} = D_{Sr}\exp\{-910.17\,E^{2+}\,[0.01255\,r_0^{2+} + 0.01575]/T\} \qquad (8c)$$

$$D_{Eu}^{3+\,cpx/melt} = D_{Sm}\exp\{-910.17\,E^{3+}\,[0.01394\,r_0^{3+} + 0.01495]/T\} \qquad (8d)$$

$$D_{Eu}^{2+\,opx/melt} = D_{Sr}\exp\{-910.17\,E^{2+}\,[0.01175\,r_0^{2+} + 0.01381]/T\} \qquad (8e)$$

$$D_{Eu}^{3+\,opx/melt} = D_{Sm}\exp\{-910.17\,E^{3+}\,[0.01048\,r_0^{3+} + 0.00998]/T\} \qquad (8f)$$

can be used to calculate D_{Eu}^{2+} and D_{Eu}^{3+} for cpx and opx, respectively, knowing D_{Sr} and D_{Sm}. Other parameters are defined as in Eq. (1). The values for r_0^{2+}, r_0^{3+}, E^{2+} and E^{3+} can be taken from Blundy and Wood (2003), for cpx:

$$r_0^{2+} = 0.974 + 0.067X_{Ca(M2)} - 0.051X_{Al(M1)} + 0.06\ [\text{Å}], \qquad (9a)$$

$$r_0^{3+} = r_0^{2+} - 0.06\ [\text{Å}], \qquad (9b)$$

$$E^{2+} = \tfrac{2}{3}(318.6 + 6.9P - 0.036T) \qquad [\text{GPa}], \qquad (9c)$$

$$E^{3+} = 1.5\,E^{2+} \quad [\text{GPa}], \qquad (9d)$$

and for opx:

$$r_0^{2+} = 0.753 + 0.118\mathrm{Al}^{tot} + 0.144\mathrm{Ca} + 0.08\ [\text{Å}], \quad (10a)$$

$$r_0^{3+} = r_0^{2+} - 0.08\ [\text{Å}], \quad (10b)$$

$$E^{2+} = 240\ \text{GPa}, \quad (10c)$$

$$E^{3+} = 360\ \text{GPa} \quad (10d)$$

Where $X_{Ca}^{(M2)}$ and $X_{Al}^{(M1)}$ refer to the atomic fractions of Ca and Al on the cpx M2 and M1 sites, P is in GPa and T in Kelvin, Al^{tot} and Ca denote atoms per 6-oxygen formula unit in the opx structural formula.

Applying Eq. (8-10) to our and published studies for which determined D_{Eu}, D_{Sr} and D_{Sm} experimentally we calculated D_{Eu}^{2+} and D_{Eu}^{3+} for cpx and opx. We selected experimental studies forming the datasets of Sun and Liang (2012) and of Yao et al. (2012) and included more recent studies to develop complete datasets for cpx and opx. In detail the literature data come from the following sources, (i) for cpx: Hauri et al. (1994), Blundy et al. (1998), Green et al. (2000), Gaetani et al. (2003), McDade et al. (2003a,b), Pertermann et al., (2004); and (ii) for opx: Green et al. (2000), McDade et al. (2003a,b), Tuff and Gibson (2007), Yao et al. (2012), Sun and Liang (2013), Dygert et al. (2020). Partitioning experiments were screened and excluded from the dataset if they could bias the model. Criteria for accepting partitioning experiments were i) $f\mathrm{O}_2$ conditions well constrained and ii) $D_{\mathrm{Eu}}^{2+}{}_{(\mathrm{calculated})} < D_{\mathrm{Eu}\ (\mathrm{measured})} < D_{\mathrm{Eu}}^{3+}{}_{(\mathrm{calculated})}$. If $D_{\mathrm{Eu}\ (\mathrm{measured})} < D_{\mathrm{Eu}}^{2+}{}_{(\mathrm{calculated})}$ or if $D_{\mathrm{Eu}\ (\mathrm{measured})} > D_{\mathrm{Eu}}^{3+}{}_{(\mathrm{calculated})}$ would imply that Eu in the melt would be present only as Eu^{2+} or Eu^{3+} reducing Eq. (2) to the normal partition coefficient D_{Eu} (i.e., concentration of Eu in crystal vs.

concentration of Eu in melt). The appropriated recalculated data set (Table S2) was fit by Eq. (7) to obtain the equilibrium constant K for cpx and opx. By nonlinear least-square regression we obtained $K = 29.8(5.6) \times 10^{-4}$ for cpx and $K = 4.7(1.7) \times 10^{-3}$ for opx.

Fig. 8 shows measured D_{Eu} vs. predicted D_{Eu} observed values are predicted within a factor of two. Although the two models are successful to reproduce the measured D_{Eu}, the major limitation of the parameterizations of these models is their dependence on a small number of calibrating observations (n = 13 for cpx and n = 8 for opx).

4.4. Pyroxene-melt Eu partitioning as oxybarometer

Eq. (7) can be rewritten to explicit fO_2 as a function of the predicted di- and tri-valent Eu partition coefficients, equilibrium constant K and measured D_{Eu} value (Wilke and Behrens, 1999; Dygert et al., 2020):

$$\log fO_2 = -4 \log[(D_{Eu}^{3+} - D_{Eu}) / (K (D_{Eu} - D_{Eu}^{2+}))]. \quad (11)$$

If measured, a D_{Eu} < predicted D_{Eu}^{2+} or measured D_{Eu} > predicted D_{Eu}^{3+} the above expression gives a meaningless result. In Fig. (9) experimental fO_2 values are plotted against predicted fO_2 values. For most of the experiments the predicted fO_2 values are within two log units of the experimental fO_2 values and it can be concluded that the models are in good agreement with the experimental data. Europium partitioning in pyroxenes seems to be a promising tool for estimating the redox conditions in natural magmatic systems. However, additional experimental data are needed to expand the

dataset, to explore the effect of other parameters such as melt composition, and to refine the quality of the fit before Eu partition coefficients between pyroxenes and melt can be applied as a robust oxybarometer in magmatic rocks. We propose the following approach to estimate fO_2: (i) measurement of pyroxene major element composition; (ii) determination of pyroxene/melt (or matrix) partition coefficients including Sr, Eu, and Sm; (iii) estimation of T and P conditions using an appropriate pyroxene thermobarometer (see review in Putirka, 2008); (iv) estimation of D_{Eu}^{2+} and of D_{Eu}^{3+} using Eq. (8); (v) application of Eq. (11) to calculate fO_2. The main condition to obtain meaningful results is that only compositions and D values representing true equilibrium between pyroxenes and coexisting melt should be used.

5. Conclusions

We measured mineral-melt partition coefficients for cpx and opx in a Fe-free basaltic system with the aim to study the effect of fO_2 on some heterovalent elements, namely Eu, Ni and Co. Application of lattice strain theory to the measurements affords a means for estimating partition coefficients for Eu^{2+} and Eu^{3+} other than for highly incompatible elements such as La. Our experimental determinations of REE partition coefficients are largely consistent with published predictive partitioning models between cpx, opx and basaltic melts. By combining the new experimental observation, literature datasets for cpx and opx, and predictive models for partitioning, we parameterized predictive models for pyroxene-melt Eu partitioning as a function of fO_2. The new models can be applied as Eu in cpx-melt or opx-melt oxybarometers in cases where equilibrium between pyroxenes and melt is proofed.

Acknowledgements

This research was supported by the Grant Agency of Czech Republic (GAČR, grant number 18-01982S to AF). Václav Špillar is thanked for his help with the regression of data.

References

Aigner-Torres, M., Blundy, J., Ulmer, P., Pettke, T., 2007. Laser Ablation ICPMS study of trace element partitioning between plagioclase and basaltic melts: an experimental approach. Contrib. Mineral. Petrol. 153, 647-667.

Arzilli, F., Fabbrizio, A., Schmidt, M.W., Petrelli, M., Maimaiti, M., Dingwell, D.B., Paris, E.,Burton, M., Carroll, M.R., 2018. The effect of diffusive re-equilibration time on trace element partitioning between alkali feldspar and trachytic melts. Chem. Geol. 495, 50-66.

Baziotis, I., Xydous, S., Asimov, P.D., Mavrogonatos, C., Flemetakis, S., Klemme, S., Berndt, J., 2019. The potential of phosphorus in clinopyroxene as a geospeedometer: Examples from mantle xenoliths. Geochim. Cosmochim. Ac. 266, 307-331.

Beattie, P., 1994. Systematics and energetics of trace-element partitioning between olivine and silicate melts – Implications for the nature of mineral melt partitioning. Chem. Geol. 117, 57-71.

Blundy, J.D., Robinson, J.A.C., Wood, B.J., 1998. Heavy REE are compatible in clinopyroxene on the spinel lherzolite solidus. Earth Planet. Sci. Lett. 160, 493-504.

Blundy, J., Wood, B., 1994. Prediction of crystal/melt partition coefficients from elastic moduli. Nature 372, 452-454.

Blundy, J., Wood, B., 2003. Mineral-melt partitioning of uranium, thorium and their daughters, in: Bourdon, B., Henderson, G.M., Lundstrom, C.C., Turner, S.P. (Eds.), Uranium-Series Geochemistry, Rev. Mineral. Geochem. 52, 59-123.

Bohlen, S.R., Essene, E.J., Boettcher, A.L., 1980. Reinvestigations and applications of olivine-quartz-orthopyroxene barometry. Earth Planet. Sc. Lett. 47, 1-10.

Bose, K., Ganguly, J., 1995. Quartz-coesite revisited: reversed experimental determinations at 500-1000 °C and retrieved thermochemical properties. Am. Mineral. 80, 231-238.

Brey, G.P., Köhler, T., 1990. Geothermobarometry in 4-phase lherzolites .2. New thermobarometers, and practical assessment of existing thermobarometers. J. Petrol 31, 1353-1378.

Brice, J.C., 1975. Some thermodynamic aspects of the growth of strained crystals. J. Crystal Growth 28, 249-253.

Burnham, A.D., Berry, A.J., 2012. An experimental study of trace element partitioning between zircon and melt as a function of oxygen fugacity. Geochim. Cosmochim. Ac. 95, 196-212.

Carmichael, I.S.E., 1991. The redox states of basic and silicic magmas – a reflection of their source regions. Contrib. Mineral. Petrol. 106, 129-141.

Cartier, C., Hammouda, T., Doucelance, R., Boyet, M., Devidal, J.L. Moine, B., 2014. Experimental study of trace element partitioning between enstatite and melt in enstatite chondrites at low oxygen fugacities and 5 GPa. Geochim. Cosmochim. Ac. 130, 167-187.

Dalou, C., Boulon, J., Koga, K.T., Dalou, R., Dennen, R.L., 2018. DOUBLE FIT:

Optimization procedure applied to lattice strain model. Comput. Geosci.-UK 117, 49-56.

Drake, M.J., 1975. The oxidation state of europium as an indicator of oxygen fugacity. Geochim. Cosmochim. Ac. 39, 55-64.

Dygert, N., Liang, Y., Sun, C., Hess, P., 2014. An experimental study of trace element partitioning between augite and Fe-rich basalts. Geochim. Cosmochim. Ac. 132, 170-186.

Dygert, N., Draper, D.S., Rapp, J.F., Lapen, T.J., Fagan, A.L., Neal, C.R., 2020. Experimental determinations of trace element partitioning between plagioclase, pigeonite, olivine, and lunar basaltic melts and an fO_2 dependent model for plagioclase-melt Eu partitioning. Geochim. Cosmochim. Ac. 279, 258-280.

Frei, D., Liebscher, A., Franz, G., Wunder, B., Klemme, S., Blundy, J., 2009. Trace element partitioning between orthopyroxene and anhydrous silicate melt on the lherzolite solidus from 1.1 to 3.2 GPa and 1230 to 1535 degrees C in the model Na_2O-CaO-MgO-Al_2O_3-SiO_2. Contrib. Mineral. Petrol. 157, 473-490.

Frost, B.R., 1991. Introduction to oxygen fugacity and its petrological importance, in: Lindsley, D.H. (Ed.), Oxide Minerals: Petrological and magnetic significance, Rew. Mineral. Geochem. 25, 1-9.

Gaetani, G., Kent, A., Grove, T., Hutchenson, I., Stolper, E., 2003. Mineral/melt partitioning of trace elements during hydrous peridotite partial melting. Contrib. Mineral. Petrol. 145, 391-405.

Green, T.H., Blundy, J.D., Adam, J., Yaxley, G.M., 2000. SIMS determination of trace element partition coefficients between garnet, clinopyroxene, hydrous basaltic liquids at 2-7.5 GPa, and 1080-1200 °C. Lithos 53, 165-187.

Günther, D., Frischknecht, R., Heinrich, C., Kahlert, H., 1997. Capabilities of an

argon fluoride 193 nm excimer laser for laser ablation inductively couples plasma mass spectrometry microanalysis of geological materials. J. Anal. At. Spectrom. 12, 939-944.

Hauri, E.H., Wagner, T.P., Grove, T.L., 1994. Experimental and natural partitioning of Th-U-Pb and other trace elements between garnet clinopyroxene and basaltic melts. Hem. Geol. 117, 149-166.

Longerich, H.P., Jackson, S.E., Günther, D., 1996. Laser ablation inductively coupled plasma mass spectrometric transient signal data acquisition and analyte concentration calculation. J. Anal. At. Spectrom. 11, 899-904.

Mallmann, G., O'Neill, H.St.C., 2007. The effect of oxygen fugacity on the partitioning of Re between crystals and silicate melt during mantle melting. Geochim. Cosmochim. Ac. 71, 2837-2857.

McDade, P., Blundy, J.D., Wood, B.J., 2003a. Trace element partitioning on the Tinaquillo lherzolite solidus at 1.5 GPa. Phys. Earth Planet. Int. 139, 129-147.

McDade, P., Blundy, J.D., Wood, B.J., 2003b. Trace element partitioning between mantle wedge peridotite and hydrous MgO-rich melt. Am. Mineral. 88, 1825-1831.

McKay, G., Le, L., Wagstaff, J., Crozaz, G., 1994. Experimental partitioning of rare earth elements and strontium: Constraints on petrogenesis and redox conditions during crystallization of Antarctic angrite Lewis Cliff 86010. Geochim. Cosmochim. Ac. 13, 2911-2919.

O'Neill, H.S., Nell, J., 1997. Gibbs free energies of formation o RuO_2, IrO_2, and OsO_2: A high-temperature electrochemical and calorimetric study. Geochim. Cosmochim. Ac. 61, 5279-5293.

Padilla, A.J., Gualda, G.A.R., 2016. Crystal-melt elemental partitioning in silicic

magmatic systems: An example from the Peach Spring Tuff high-silica rhyolite, Southwest USA. Chem. Geol. 440, 326-344.

Paton, C., Hellstrom, J., Paul, B., Woodhead, J., Hergt, J., 2011. Iolite: Freeware for the visualization and processing of mass spectrometric data. J. Anal. At. Spectrom. 26, 2508-2518.

Petrelli, M., Caricchi, L., Ulmer, P., 2007. Application of high spatial resolution laser ablation ICP-MS to crystal-melt trace element partition coefficient determination. Geostand. Geoanal. Res. 31, 13-25.

Petrelli, M., Perugini, D., Alagna, K.E., Poli, G., Peccerillo, A., 2008. Spatially resolved and bulk trace element analysis by laser ablation – inductively coupled plasma – mass spectrometry (LA-ICP-MS). Period. Mineral. 77, 3-21.

Petrelli, M., Laeger, K., Perugini, D., 2016a. High spatial resolution trace element determination of geological samples by laser ablation quadrupole plasma mass spectrometry: implications for glass analysis in volcanic products. Geosci. J. 20, 851-863.

Petrelli, M., Morgavi, D., Vetere, F., Perugini, D., 2016b. Elemental imaging and petro-volcanological applications of an improved Laser Ablation Inductively Coupled Quadrupole Plasma Mass Spectrometry. Period. Mineral. 85, 25-39.

Pertermann, M., Hirschmann, M.M., Hametner, K., Günther, D., Schmidt, M.W., 2004. Experimental determination of trace element partitioning between garnet and silica-rich liquid during anhydrous partial melting of MORB-like eclogite. Geochem. Geophys. 5, Q05A01 doi: 10.1029/2003GC000638.

Pinilla, C., Davis, S.A., Scott, T.B., Allan, N.L., Blundy, J.D., 2012. Interfacial storage of noble gases and other trace elements in magmatic systems. Earth Planet. Sci. Lett. 319, 287-294.

Pownceby, M.I., O'Neill, H.S.C., 1994. Thermodynamic data from redox reactions at high temperatures. IV. Calibration of the Re-ReO_2 oxygen buffer from EMF and NiO+Ni-Pd redox sensor measurements. Contrib. Mineral. Petrol. 118, 130-137.

Putirka, K.D., 2008. Thermometers and Barometers for Volcanic Systems, in: Putirka, K.D., Tepley, F.J. (Eds.), Minerals, Inclusions and Volcanic Processes, Rev. Mineral. Geochem. 69, 61-120.

Salters, VJ.M., Longhi, J.E., Bizimis, M., 2002. Near mantle solidus trace element partitioning at pressures up to 3.4 GPa. Geochem. Geophys. 3, 1038 doi: 10.1029/2001GC000148.

Shannon, R.D., 1976. Revised effective ionic radii and systematic studies of interatomic distances in halides and chalcogenides. Acta Crystallogr. A A32, 751-767.

Shearer, C.K., Papike, J.J., Karner, J.M., 2006. Pyroxene europium valence oxybarometer: Effects of pyroxene composition, melt composition, and crystallization kinetics. Am. Mineral. 91, 1565-1573.

Sun, C., 2018. Partitioning and Partition Coefficients, in: Encyclopedia Of Geochemistry. https://doi.org/10.1007/978-3-319-39193-9.

Sun, C., Liang, Y., 2012. Distribution of REE between clinopyroxene and basaltic melt along a mantle adiabat: effects of major element composition, water, and temperature. Contrib. Mineral. Petrol. 163, 807-823.

Sun, C., Liang, Y., 2013. Distribution of REE and HFSE between low-Ca pyroxene and lunar picritic melts around multiple saturation points. Geochim. Cosmochim. Ac. 119, 340-358.

Tiepolo, M., Obert, R., Zanetti, A., Vannucci, R., Foley, S.F., 2007. Trace-element

partitioning between amphibole and silicate melt, in: Hawthorne, F.C., Oberti, R., DellaVentura, G., Mottana, A. (Eds.), Amphiboles: Crystal Chemistry, Occurrence, and Health Issues, Rev. Mineral. Geochem. 67, 417-451.

Trail, D., Watson, E.B., Tailby, N.D., 2011. The oxidation state of Hadean magmas and implications for early Earth's atmosphere. Nature 480, 79-U238.

Trail, D., Watson, E.B., Tailby, N.D., 2012. Ce and Eu anomalies in zircon as proxies for the oxidation state of magmas. Geochim. Cosmochim. Ac. 97, 70-87.

Tuff, J., Gibson, S.A., 2007. Trace-element partitioning between garnet, clinopyroxene and Fe-rich picritic melts at 3 to 7 GPa. Contrib. Mineral. Petrol. 153, 369-387.

van Kan Parker, M., Liebscher, A., Frei, D., van Sijl, J., van Westrenen, W., Blundy, J., Franz, G., 2010. Experimental and computational study of trace element distribution between orthopyroxene and anhydrous silicate melt: substitution mechanisms and the effect of iron. Contrib. Mineral. Petrol. 159, 459-473.

van Kan Parker, M., Mason, P.R.D., van Westrenen, W., 2011. Experimental study of trace element partitioning between lunar orthopyroxene and anhydrous silicate melt: Effects of lithium and iron. Chem. Geol. 285, 1-14.

Weill, D.F., McKay, G., A., Kriedelbaugh, S.J., Grutzeck, M., 1974. Modeling the evolution of Sm and Eu abundances during lunar igneous differentiation. Proc. 5th Lunar Plan. Sci. Conf. 2, 1337-1352.

Wilke, M., Behrens, H., 1999. The dependence of the partitioning of iron and europium between plagioclase and hydrous tonalitic melt on oxygen fugacity. Contrib. Mineral. Petrol. 137, 102-114.

White, J.C., Holt, G.S., Parker D.F., Ren, M.H., 2003. Trace-element partitioning

between alkali feldspar and peralkalic quartz trachyte to rhyolite magma. Part I: Systematics of trace-element partitioning. Am. Mineral. 88, 316-329.

Yao, L., Sun, C., Liang, Y., 2012. A parameterized model for REE distribution between low-Ca pyroxene and basaltic melts with applications to REE partitioning in low-Ca pyroxene along a mantle adiabat and during pyroxenite-derived melt and peridotite interaction. Contrib. Mineral. Petrol. 164, 261-280.

Figure and table captions

Fig. 1. Backscattered electron images of experimental run products. Scale bars are 100 μm. Abbreviations: cpx = clinopyroxene, opx = orthopyroxene, fo = forsterire, sp = spinel. (a) Run 21, the black frame is the graphite capsule. The opx crystal on the top of the charge shows micrometer acicular quench rims. (b) Run 23, the white borders are the Pt capsule whereas the white on the bottom is the $RuRuO_2$ buffer. (c) Run 24, the white borders are the Pt capsule whereas the white on the top is the $ReReO_2$ buffer. (d) Run 25, the black frame is the graphite capsule. Cpx grains show a micrometer quench rim zoning.

Fig. 2. Experimental temperature plotted against temperature calculated using the opxe-only (squares) and cpx-opx (circles) geothermometer of Brey and Köhler (1990) for runs with coexisting cpx and opx. The black solid line is the 1:1 line.

Fig. 3. (a) Measured partition coefficients, arranged in geochemical groups with

increasing compatibility. LILE stands for large ion lithophile element; REE+Y stands for rare earth elements plus yttrium; HFSE stands for high field strength element; TM stands for transition metal; cpx and opx stand respectively for cpx and opx. (b) Enlargement of REE+Y section reported in part (a). Filled symbols: cpx; open and half-filled symbols: opx; circles: run 13; half-filled diamonds: run 16; squares: run 21; diamonds: run 23; half-filled squares: run 24; triangles: run 25.

Fig. 4. Onuma diagrams showing partition coefficients for di-, tri-, and tetra-valent cations between cpx and melt as a function of ionic radii (a-d). The partitioning data are from runs 13 (a), 21 (b), 23 (c) and 25 (d) reported in this study. The horizontal lines represent the size range of the M1 (open arrows) and M2 (closed arrows) sites. Open symbols: elements entering in the M1 site. Closed symbols: elements entering in the M2 site. Diamonds: divalent elements; squares: trivalent elements; triangles: tetravalent elements. Semi-filled symbols: D_{Eu} values as calculated from the LA-ICP-MS analyses plotted against its di- and tri-valent ionic radii, these values are excluded from the fits. The partition coefficients for di- (Eu^{2+}) and tri- (Eu^{3+}) valent Eu are calculated as explained in the text and included in the fits. The partition coefficients for Al are calculated considering the Al content in the M1 site. Errors bars represent one standard deviation of partitioning data. Barium partition coefficients are not included in the fits, see main text. The solid lines represent the best-fit parabolas to isovalent elements in the M1 and M2 sites of cpx using Eq. (1). Ionic radii in VI-fold and VIII-fold coordination in, respectively,

the M1 and M2 sites are taken from Shannon (1976). The lattice strain parameters for all runs are listed in Table 4.

Fig. 5. Measured REE+Y cpx-melt partition coefficients (a) plotted against those calculated using the model of Sun and Liang (2012) and measured REE+Y opx-melt partition coefficients (b) plotted against those calculated using the model of Yao et al. (2012). Symbols as in Fig. 3. The solid lines are 1:1, dashed lines are 1:2 and 2:1.

Fig. 6. Onuma diagrams showing partition coefficients for di-, tri-, and tetra-valent cations between opx and melt as a function of ionic radii (a-f). The partitioning data are from runs 13 (a), 16 (b), 21 (c), 23 (d), 24 (e) and 25 (f) reported in this study. The horizontal lines represent the size range of the M1 (open arrows) and M2 (closed arrows) sites. Symbols as in Figure 4. The partition coefficients for di- (Eu^{2+}) and tri- (Eu^{3+}) valent Eu are calculated as explained in the text and included in the fits. The partition coefficients for Al are calculated considering the Al content in the M1 site. Errors bars represent one standard deviation of partitioning data. Barium partition coefficients are not included in the fits, see main text. The solid lines represent the best-fit parabolas to isovalent elements in the VI-fold coordinated M1 and M2 sites of opx using Eq. (1). Ionic radii are taken from Shannon (1976). The lattice strain parameters for all runs are listed in Table 4.

Fig. 7. Variation of Ni (diamonds), Co (squares) and Eu (circles) partition coefficients in (a) cpx and (b) in opx as a function of the experimental fO_2.

Fig. 8. Measured Eu distribution coefficients for cpx (closed circles) and opx (open circles) plotted against D_{Eu} values predicted using Eq. (7). Solid line is 1:1; dashed lines are 1:2 and 2:1. In general the experimental observations are reproduced within a factor or two or better both for cpx and opx.

Fig. 9. Experimentally imposed oxygen fugacity plotted against predicted fO_2 using Eq. (19). Closed circles: cpx. Open circles: opx. The solid line is 1:1, dashed lines are predicted fO_2 values two order of magnitude above and below experimental fO_2. Most of the experimentally imposed fO_2 are well predicted within two order of magnitude.

Table 1. Starting material composition.

Table 2. Run conditions, electron microprobe and laser ablation analyses.

Table 3. Pyroxene-melt partition coefficients.

Table 4. List of lattice strain parameters for individual experiments, their estimation by the relations of Blundy and Wood (2003) and proportions of Eu^{2+} to total Eu in melt (XEu^{2+}_{melt}).

Supplementary material. Estimation of D_{Eu}^{2+} and D_{Eu}^{3+} in pyroxenes.

Fig. S1. Proportion of Eu^{2+} to total Eu in melt, $X(Eu^{2+})_{melt}$, calculated with data of

clinopyroxene (circles) and of orthopyroxene (squares), as a function of experimental fO_2.

Table S1. Trace elements concentration (ppm) in the starting composition.

Table S2. Data sources and experimental run conditions.

Figure 1

Click here to download high resolution image

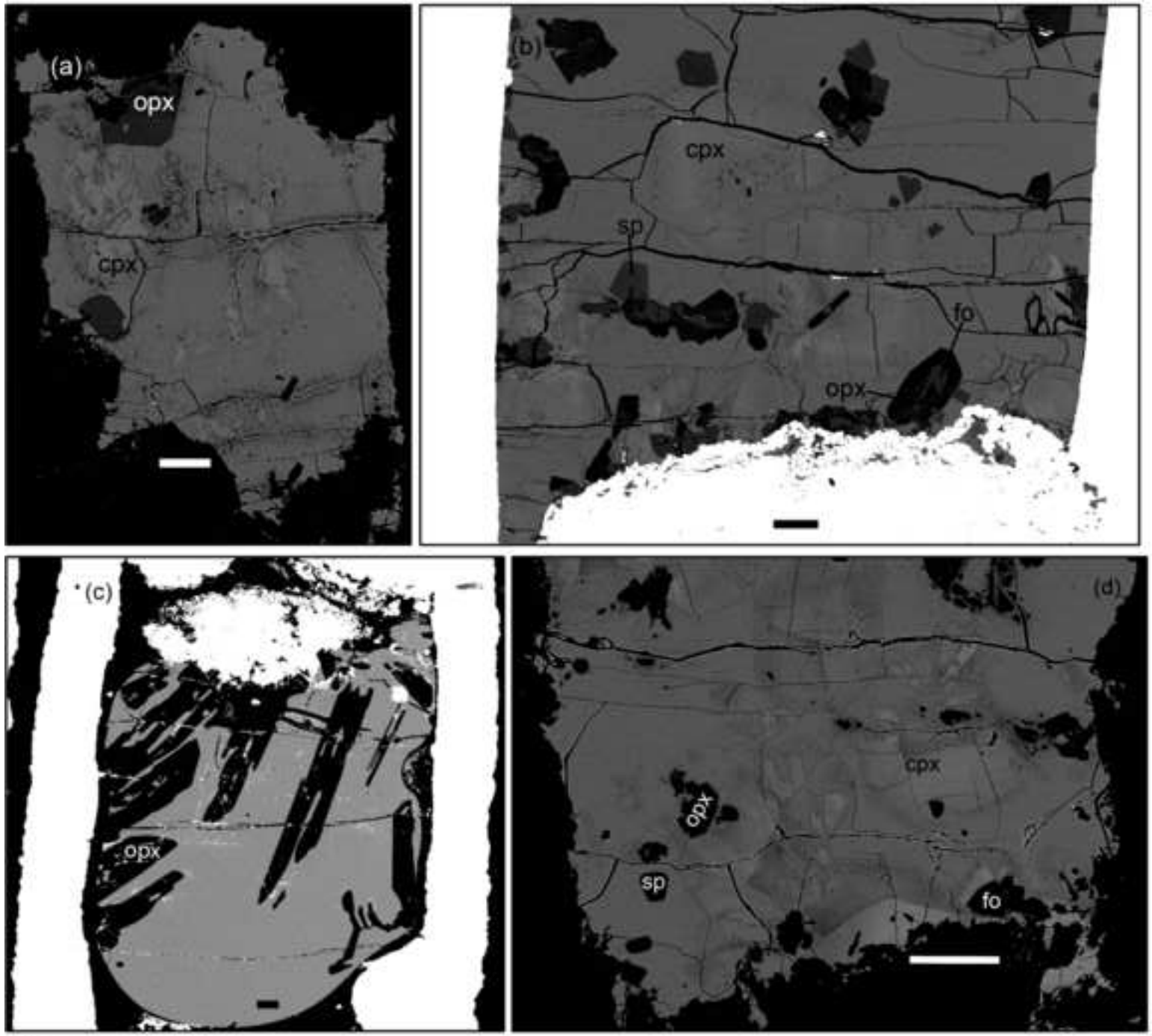

Figure 1

Figure 2

Click here to download high resolution image

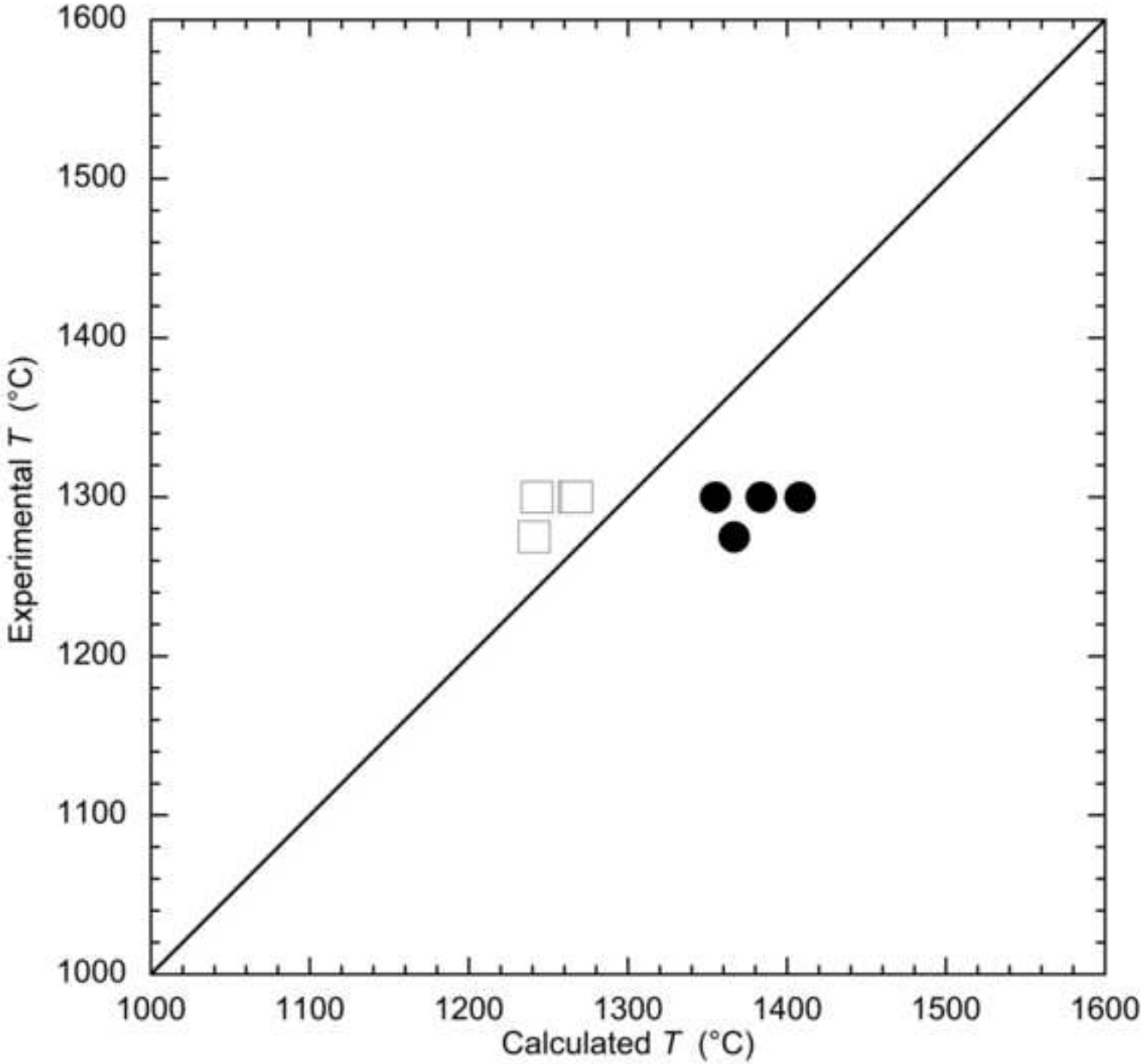

Figure 3

Click here to download high resolution image

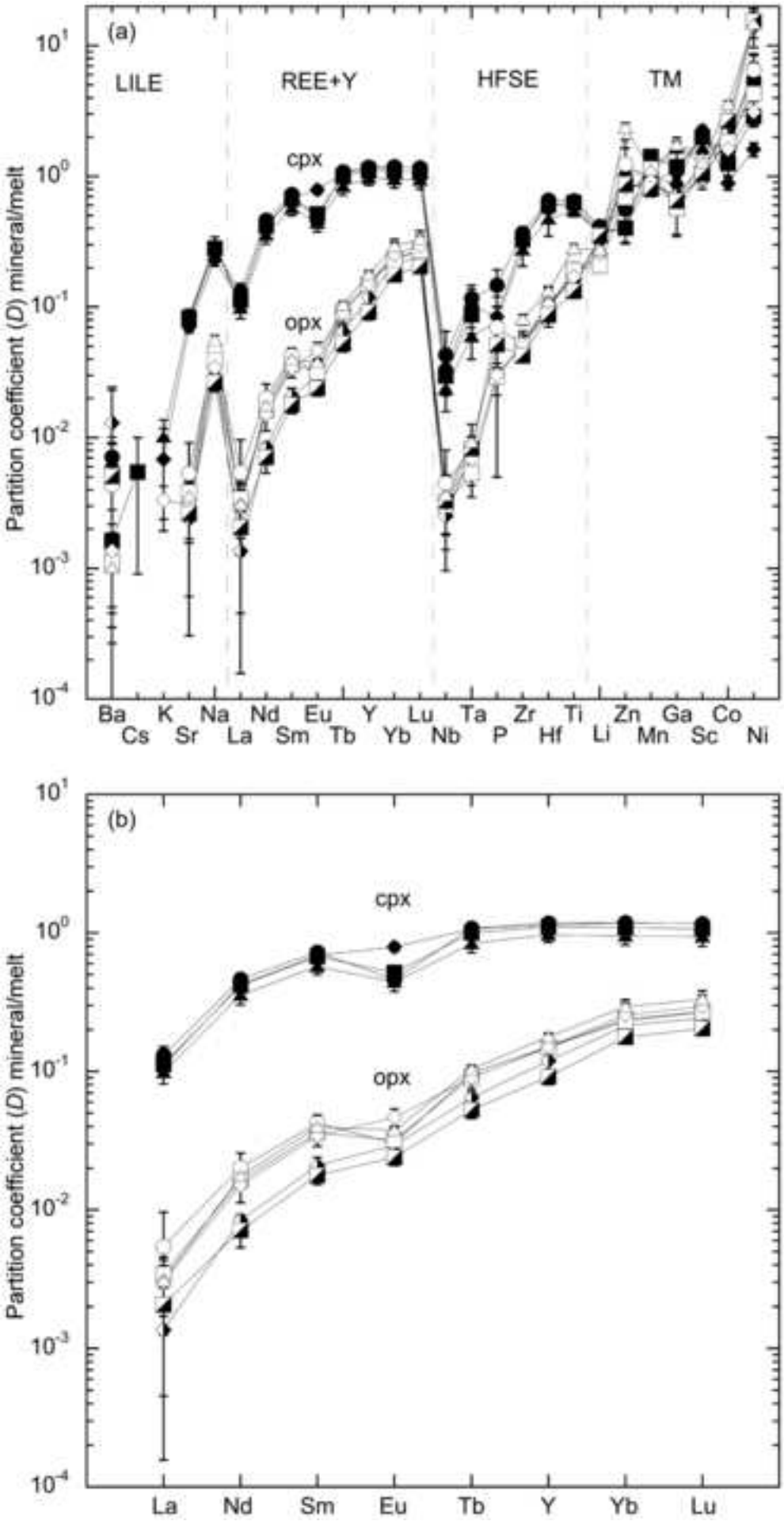

Figure 4

Click here to download high resolution image

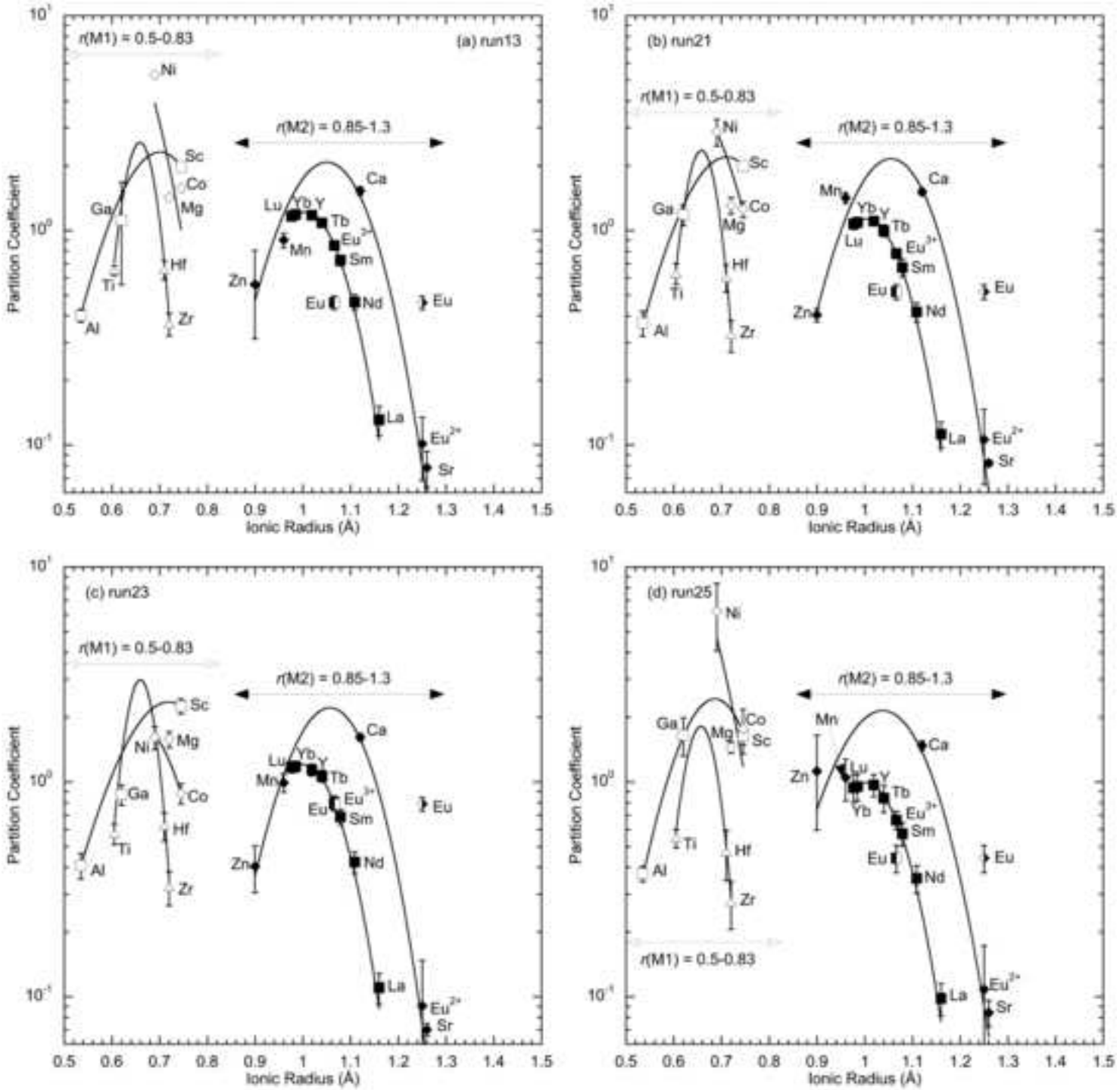

Figure 5

Click here to download high resolution image

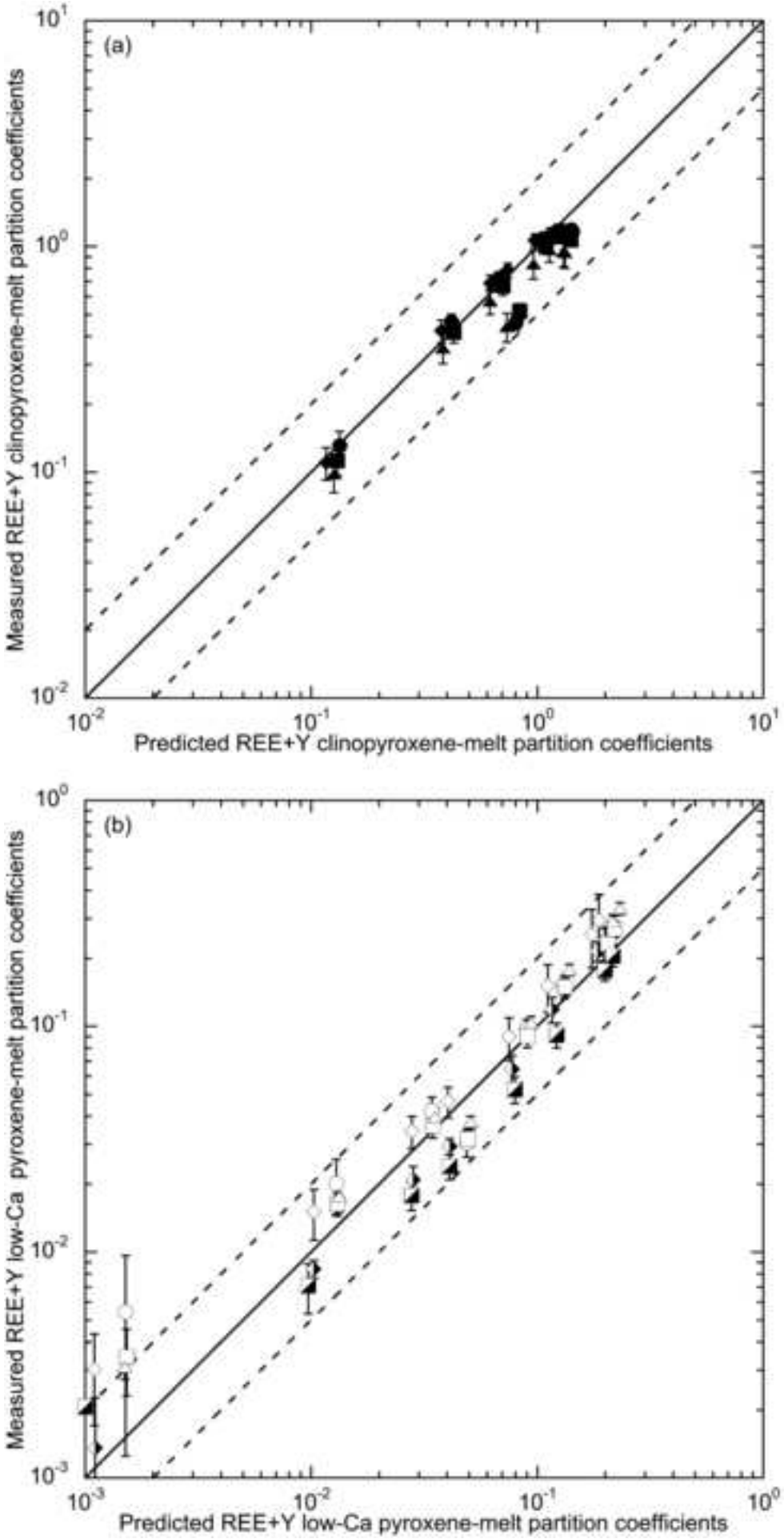

Figure 6

Click here to download high resolution image

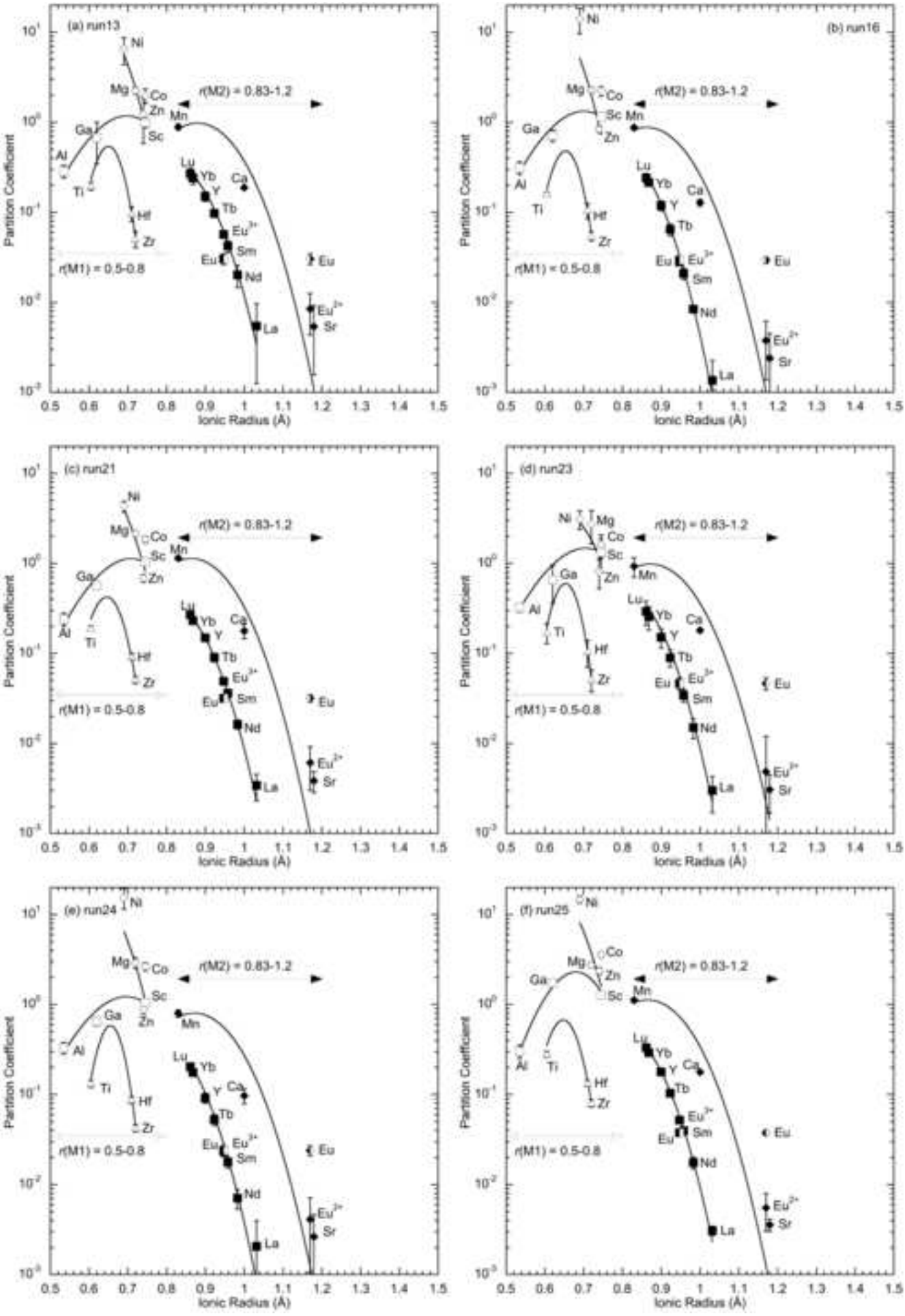

Figure 7

Click here to download high resolution image

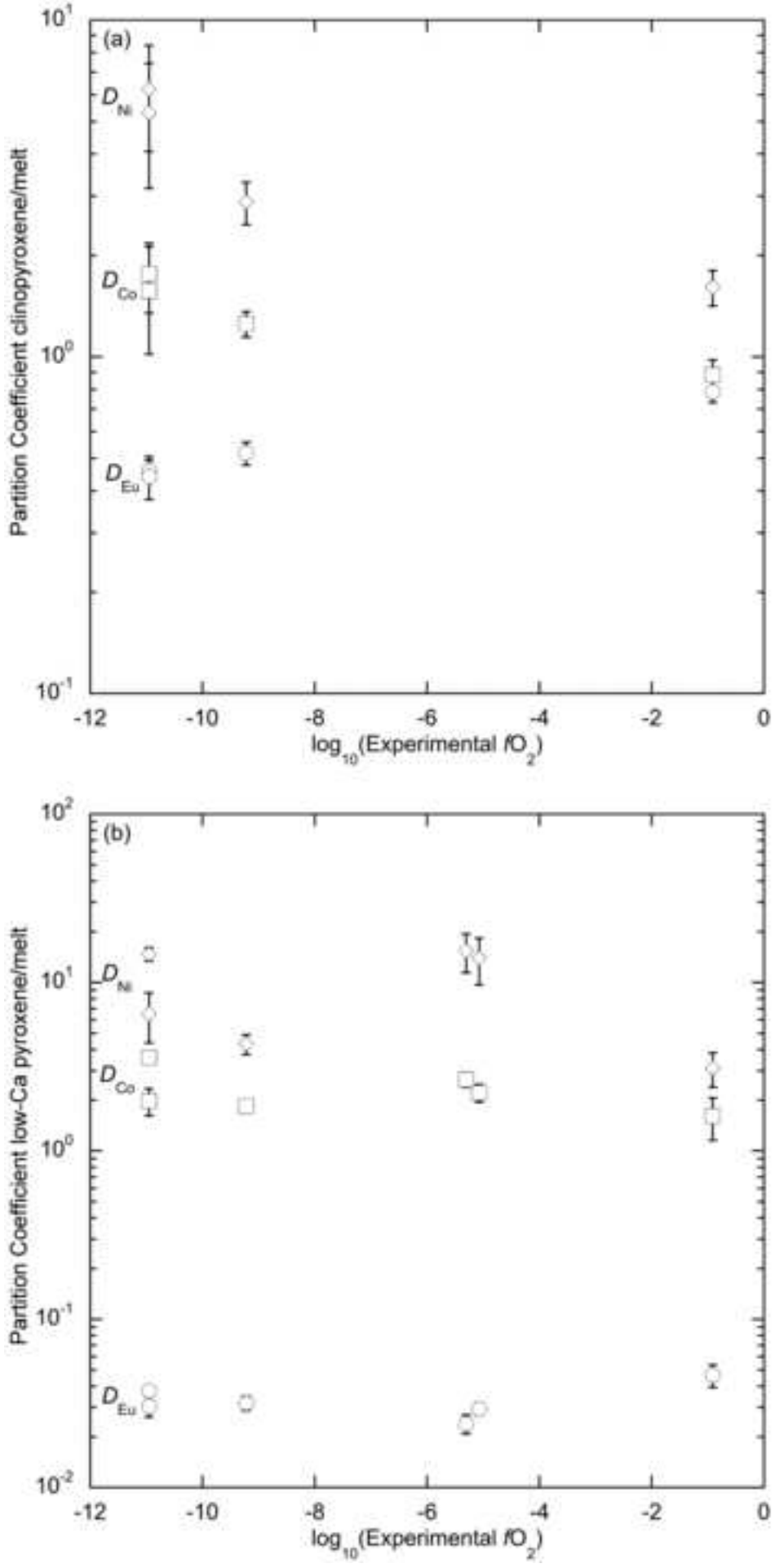

Figure 8

Click here to download high resolution image

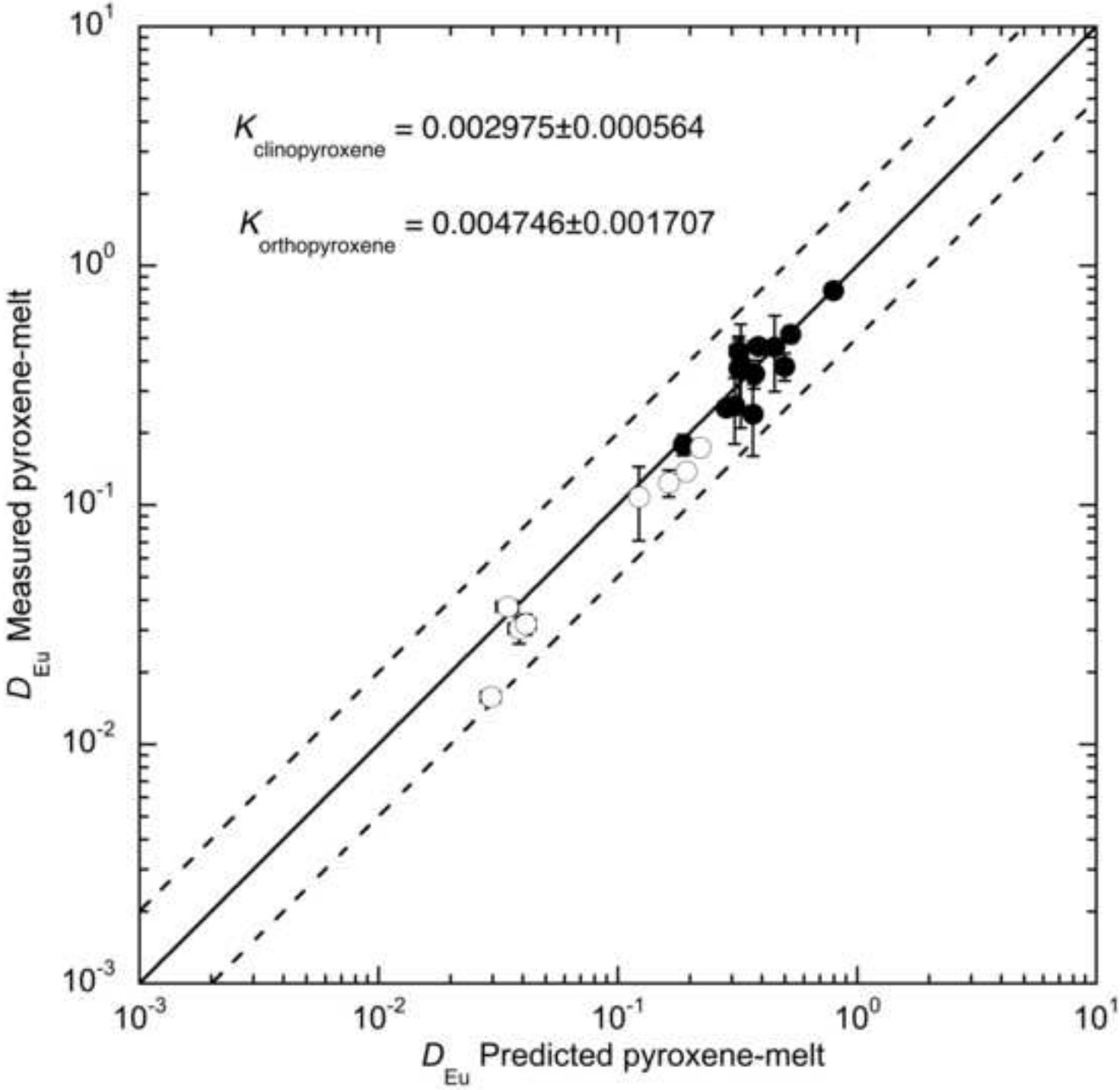

Figure 9

Click here to download high resolution image

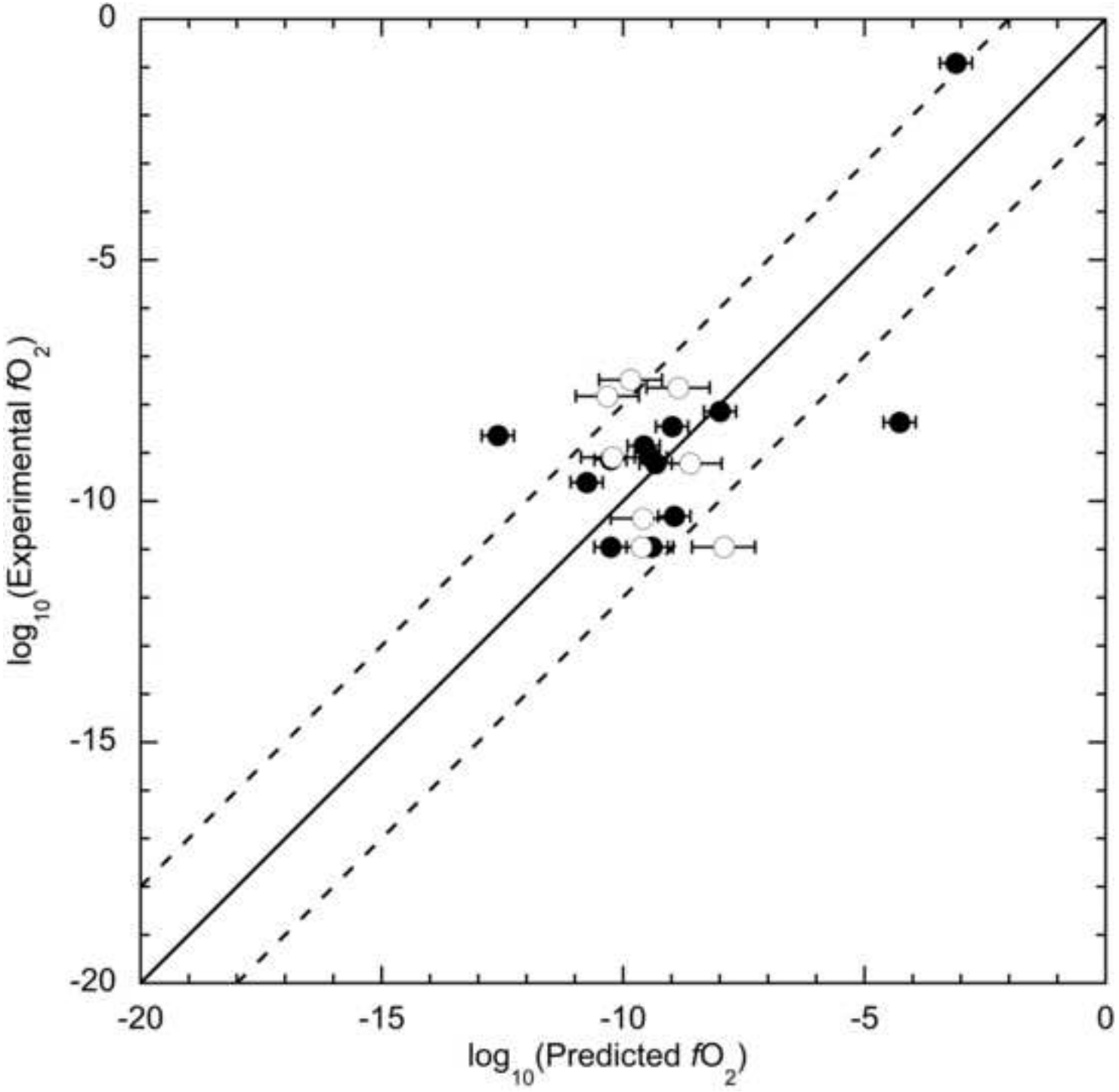

Table 1
Starting material composition.

	Starting composition[a]	BASE (Mallmann and O'Neill 2007)
SiO_2	47.3	48.3
TiO_2	1.28	1.30
Al_2O_3	18.7	19.1
MnO	0.18	0.18
MgO	15.6	15.9
CaO	11.4	11.6
Na_2O	2.43	2.48
K_2O	0.11	0.10
P_2O_5	0.15	0.15
NiO	0.98	-
CoO	0.97	-
TrE[b]	1.01	0.88
Total	100.11	99.99

Note: [a]Calculated weight percent oxide equivalent based on mixture prepared from oxide, carbonate and phosphate powders. [b]TrE: trace elements.

Table 2

Click here to download Table: Table 2.docx

Table 2

Run conditions, electron microprobe and laser ablation analyses.

Run#	13			16		21			23			24		25		
T (°C)/*P*(GPa)	1300/1.5			1300/1.5		1300/1.5			1275/1.5			1275/1.5		1300/1.5		
Buffer	CMO			$ReReO_2$		CCO			$RuRuO_2$			$ReReO_2$		CMO		
logfO_2	-10.95			-5.07		-9.22			-0.91			-5.30		-10.95		
Time (h) at final *T*	26			48		53			43			44.5		48		
Assemblage	cpx,opx,fo,sp			opx		cpx,opx			cpx,opx,fo,sp			opx		cpx,opx,fo,sp		
EMPA (wt%)																
Phase	cpx	opx	gl	opx	gl	cpx	opx	gl	cpx	opx	gl	opx	gl	cpx	opx	gl
n	16	6	16	9	10	6	4	10	17	10	10	9	8	9	3	8
SiO_2	46.85 (56)	51.84 (69)	48.99 (20)	51.26 (89)	47.64 (24)	46.21 (64)	51.54 (38)	47.72 (17)	47.28 (80)	52.74 (35)	48.15 (30)	49.25 (74)	50.65 (29)	48.13 (84)	51.15 (57)	48.28 (20)
TiO_2	1.15 (10)	0.42 (3)	1.53 (5)	0.23 (3)	1.40 (6)	1.01 (11)	0.33 (4)	1.45 (4)	0.95 (13)	0.32 (2)	1.61 (4)	0.26 (4)	1.70 (5)	0.96 (8)	0.36 (5)	1.53 (7)
Al_2O_3	15.60 (52)	11.58 (88)	19.66 (11)	12.37 (99)	19.10 (11)	14.96 (93)	10.47 (76)	19.10 (12)	15.02 (99)	11.51 (57)	19.1 (9)	13.95 (95)	20.61 (8)	14.39 (60)	12.54 (98)	19.66 (11)
MnO	0.15 (2)	0.16 (1)	0.17 (2)	0.14 (1)	0.17 (3)	0.14 (1)	0.14 (1)	0.12 (1)	0.17 (1)	0.18 (1)	0.18 (2)	0.15 (2)	0.18 (2)	0.19 (3)	0.23 (2)	0.21 (3)
MgO	17.34 (82)	32.97 (31)	12.27 (12)	32.54 (76)	14.06 (11)	17.68 (80)	34.04 (51)	13.75 (13)	16.30 (70)	30.85 (19)	10.34 (9)	31.11 (62)	9.67 (15)	18.74 (61)	32.98 (59)	12.52 (9)
CaO	16.78 (76)	2.06 (29)	10.99 (9)	1.40 (12)	10.96 (6)	17.58 (55)	2.06 (38)	11.61 (8)	17.20 (63)	1.92 (8)	10.66 (10)	1.02 (19)	10.51 (7)	15.99 (36)	1.93 (8)	11.12 (14)
Na_2O	0.80 (3)	0.15 (1)	3.24 (5)	0.04 (1)	1.07 (4)	0.73 (2)	0.13 (2)	2.82 (6)	0.81 (3)	0.14 (1)	3.66 (8)	0.03 (1)	0.96 (1)	0.82 (3)	0.14 (5)	3.09 (5)
K_2O	-	-	0.21 (2)	-	0.03 (1)	-	-	0.16 (1)	-	-	0.22 (2)	-	0.03 (1)	-	-	0.21 (2)
P_2O_5	-	-	0.11 (2)	-	0.01 (2)	-	-	0.10 (4)	-	-	0.17 (3)	-	0.05 (3)	-	-	0.12 (3)
NiO	0.02 (1)	0.03 (1)	0.01 (1)	0.81 (31)	0.07 (1)	0.01 (1)	0.01 (1)	0.01 (1)	0.78 (6)	1.64 (7)	0.38 (1)	1.03 (10)	0.06 (1)	0.09 (1)	0.15 (2)	0.02 (1)
CoO	0.08 (3)	0.13 (1)	0.05 (2)	0.92 (12)	0.43 (1)	0.11 (1)	0.20 (1)	0.08 (1)	0.69 (3)	1.38 (2)	0.74 (1)	1.18 (9)	0.38 (1)	0.25 (1)	0.42 (5)	0.12 (1)
Total	98.8 (31)	99.3 (48)	97.2 (43)	99.8 (52)	94.9 (50)	98.5 (38)	98.9 (42)	96.9 (21)	99.2 (45)	100.7 (30)	95.3 (44)	98.0 (23)	94.8 (26)	99.5 (16)	99.9 (21)	96.9 (29)
Wo	41	4		3		42	4		43	4		2		37	4	
En	59	96		97		58	96		47	96		98		63	96	
LA-ICP-MS (ppm)																
n	6	4	5	5	5	4	3	5	23	11	5	10	5	5	3	5
Li	50 (3)	27 (3)	120 (2)	27 (5)	82 (1)	47 (2)	26 (2)	124 (3)	53 (5)	38 (7)	145 (4)	27 (2)	76 (1)	47 (7)	35 (3)	127 (6)
Na	6687 (238)	1149 (95)	2.5[a] (2)	338 (76)	8790 (217)	6565 (289)	910 (25)	2.33[a] (2)	6544 (619)	974 (231)	2.84[a] (13)	221 (32)	8350 (135)	7246 (951)	1340 (110)	2.40[a] (6)
Mg	10.9[a] (43)	17.2[a] (1.5)	7.6[a] (1)	20.7[a] (1.5)	9.1[a] (1)	11.8[a] (9)	19.5[a] (1.2)	9.0[a] (1)	11.2[a] (9)	19.5[a] (7.7)	7.1[a] (2)	19.5[a] (2.5)	6.7[a] (2)	11.6[a] (6)	22.1[a](1.4)	8.0[a] (1)
Al	8.9[a] (2)	4.8[a] (7)	11.3[a] (1)	7.5[a] (6)	11.3[a] (2)	8.3[a] (5)	5.3[a] (3)	11.1[a] (1)	9.3[a] (7)	6.7[a] (3)	11.2[a] (2)	8.2[a] (8)	12.5[a] (3)	8.0 (9)[a]	8.4 (6)[a]	11.1[a] (2)
P	129 (40)	61 (17)	876 (7)	bdl	726 (18)	bdl	22 (6)	766 (7)	86 (36)	31 (26)	1018 (40)	49 (16)	947 (20)	61 (18)	bdl	799 (21)
K	bdl	bdl	1886 (12)	bdl	203 (2)	bdl	bdl	1532 (21)	13 (9)	6.3 (1.8)	1920 (60)	bdl	257 (6)	18 (6)	bdl	1771 (43)
Sc	490 (22)	246 (29)	248 (4)	344 (20)	298 (12)	554 (23)	289 (13)	278 (3)	518 (41)	305 (121)	230 (2)	335 (27)	319 (11)	458 (38)	357 (15)	280 (12)
Ti	5861 (308)	1765 (180)	8992 (103)	1334 (40)	8320 (142)	5425 (591)	1647 (91)	8630 (130)	5309 (549)	1586 (397)	9274 (231)	1385 (125)	10486 (171)	4584 (370)	2360 (130)	8394 (468)
Mn	1239 (96)	1219 (91)	1374 (22)	1365 (77)	1567 (15)	1420 (76)	1146 (57)	1002 (23)	1523 (140)	1431 (353)	1538 (41)	1261 (113)	1579 (52)	1950 (429)	2090 (110)	1866 (28)
Co	736 (259)	928 (171)	468 (9)	0.94[a] (11)	4268 (54)	1019 (58)	1502 (86)	813 (53)	6302 (658)	1.15[a](32)	7126 (210)	1.01[a](9)	3818 (140)	1994 (465)	4050 (220)	1132 (26)
Ni	184 (73)	227 (74)	35 (2)	0.90[a] (28)	643 (10)	50 (7)	76 (10)	18 (1)	6895 (765)	1.33[a](30)	4282 (204)	8323 (1569)	539 (96)	705 (239)	1665 (97)	113 (8)
Zn	12 (5)	26 (14)	21 (1)	368 (32)	440 (12)	20 (1)	34 (3)	49 (2)	197 (47)	396 (140)	486 (26)	391 (38)	447 (13)	66 (31)	140 (10)	59 (3)
Ga	71 (35)	43 (21)	63 (3)	305 (44)	427 (6)	139 (15)	67 (5)	118 (5)	349 (35)	264 (119)	401 (16)	312 (32)	481 (14)	250 (50)	264 (14)	151 (2)
Rb	bdl	bdl	177 (1)	bdl	14 (1)	bdl	bdl	149 (2)	bdl	bdl	203 (5)	bdl	16 (1)	bdl	bdl	171 (7)
Sr	45 (8)	3.0 (2.1)	567 (16)	0.71 (0.61)	294 (5)	40 (1)	1.9 (0.5)	481 (9)	45 (3)	1.9 (0.9)	641 (15)	0.65 (0.50)	247 (3)	44 (6)	1.9 (3)	523 (15)
Y	468 (12)	60 (7)	397 (8)	51 (6)	426 (18)	449 (19)	61 (6)	407 (5)	483 (29)	64 (15)	425 (9)	51 (6)	553 (13)	412 (46)	76 (3)	426 (26)
Zr	173 (20)	24 (5)	472 (10)	22 (2)	394 (17)	137 (23)	22 (2)	422 (4)	171 (30)	27 (7)	529 (20)	22 (2)	529 (13)	130 (32)	38 (3)	473 (26)
Nb	24 (12)	2.5 (1.9)	549 (12)	1.1 (0.3)	421 (6)	13 (3)	1.3 (0.3)	435 (7)	19 (5)	1.7 (0.7)	554 (26)	1.8 (1.0)	541 (8)	12 (4)	1.8 (0.2)	493 (17)
Cs	bdl	bdl	130 (3)	bdl	6.1 (2.0)	0.6 (0.5)	bdl	112 (1)	bdl	bdl	155 (4)	bdl	6.9 (0.2)	bdl	bdl	129 (3)
Ba	4.1 (9.3)	2.5 (2.6)	580 (22)	2.5 (2.3)	195 (3)	0.8 (0.3)	0.6 (0.4)	507 (8)	3.2 (3.0)	0.9 (0.9)	679 (20)	0.8 (0.8)	152 (5)	3.6 (3.3)	0.6 (0.3)	550 (14)
La	75 (11)	3.1 (2.4)	574 (19)	0.6 (0.4)	455 (7)	56 (8)	1.7 (0.6)	502 (8)	74 (12)	2.0 (0.9)	672 (20)	1.2 (9)	569 (12)	56 (10)	1.8 (0.2)	566 (15)
Nd	225 (17)	10 (3)	485 (13)	3.7 (3)	435 (6)	194 (20)	7.6 (0.9)	465 (6)	241 (27)	8.6 (2.2)	569 (10)	3.9 (0.9)	561 (11)	182 (26)	9.0 (1.3)	512 (11)
Sm	388 (18)	23 (3)	535 (16)	11 (2)	523 (9)	365 (33)	20 (2)	543 (10)	427 (34)	21 (3)	621 (10)	12 (2)	678 (12)	331 (41)	23 (2)	577 (13)
Eu	265 (16)	17 (2)	575 (22)	15 (1)	502 (3)	282 (22)	17 (2)	544 (9)	472 (34)	28 (4)	599 (7)	14 (2)	591 (7)	258 (38)	22 (1)	585 (9)
Tb	462 (17)	42 (4)	426 (14)	30 (4)	458 (17)	456 (27)	41 (5)	457 (10)	513 (32)	43 (9)	481 (7)	32 (4)	609 (13)	400 (55)	49 (3)	477 (19)
Yb	489 (11)	99 (14)	412 (15)	99 (9)	460 (16)	497 (21)	105 (9)	456 (8)	552 (32)	119 (34)	468 (6)	106 (11)	601 (13)	448 (62)	137 (8)	471 (15)
Lu	447 (11)	103 (14)	384 (17)	104 (12)	430 (18)	455 (24)	114 (9)	424 (8)	510 (30)	128 (39)	435 (7)	117 (12)	571 (12)	414 (59)	146 (7)	441 (16)
Hf	307 (27)	46 (8)	469 (22)	47 (9)	444 (17)	281 (40)	43 (3)	466 (7)	339 (49)	57 (19)	543 (13)	53 (4)	616 (13)	247 (64)	70 (4)	524 (27)
Ta	73 (19)	5.1 (2.9)	630 (29)	3.8 (0.9)	506 (12)	48 (14)	3.1 (0.3)	552 (8)	73 (24)	4.8 (1.8)	704 (30)	5.8 (1.3)	699 (12)	38 (13)	5.9 (0.6)	645 (16)

Note: [a]wt%. n = number of analyses. Cpx = clinopyroxene. Opx = orthopyroxene. Fo = forsterite. Sp = spinel. Gl = glass. bdl = below detection limit. Number in parenthesis indicates one standard deviation*100 for major elements and one standard deviation for trace elements.